

Symmetric Volume Maps

S. MAZDAK ABULNAGA, Massachusetts Institute of Technology, USA

ODED STEIN, Massachusetts Institute of Technology, USA

POLINA GOLLAND, Massachusetts Institute of Technology, USA

JUSTIN SOLOMON, Massachusetts Institute of Technology, USA

Although shape correspondence is a central problem in geometry processing, most methods for this task apply only to two-dimensional surfaces. The neglected task of *volumetric* correspondence—a natural extension relevant to shapes extracted from simulation, medical imaging, volume rendering, and even improving surface maps of boundary representations—presents unique challenges that do not appear in the two-dimensional case. In this work, we propose a method for mapping between volumes represented as tetrahedral meshes. Our formulation minimizes a distortion energy designed to extract maps symmetrically, i.e., without dependence on the ordering of the source and target domains. We accompany our method with theoretical discussion describing the consequences of this symmetry assumption, leading us to select a symmetrized ARAP energy that favors isometric correspondences. Our final formulation optimizes for near-isometry while matching the boundary. We demonstrate our method on a diverse geometric dataset, producing low-distortion matchings that align to the boundary.

CCS Concepts: • Computing methodologies → Volumetric models; Shape analysis.

Additional Key Words and Phrases: correspondence, volumes, tetrahedral meshes, as-rigid-as-possible, symmetry

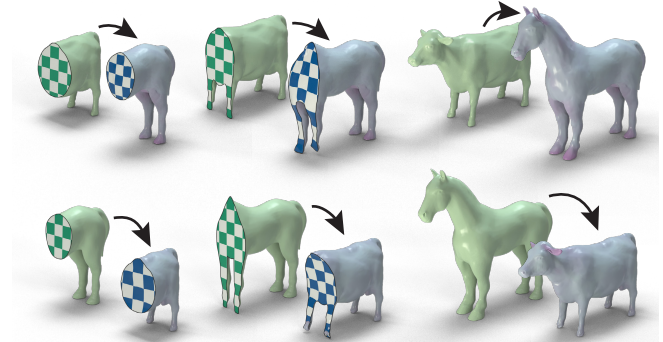
1 INTRODUCTION

Shape correspondences are at the core of many applications in graphics and geometry processing, including texture transfer, animation, statistical shape analysis, and segmentation transfer. The central objective of these applications is to compute a dense map between two input shapes, facilitating semantically-meaningful information transfer with minimal distortion.

The vast majority of shape correspondence algorithms focuses on mapping two-dimensional surfaces. These approaches leverage geometric properties that are unique to surfaces. For example, key shape properties like curvature are defined over the entire surface domain, rather than only on the boundary as in the volumetric case. As a result, one can even find reasonable correspondences by matching geometric features directly, without incorporating any notion of distortion [Ovsjanikov et al. 2010]. Other methods use Tutte’s embedding or notions of discrete conformality specific to surfaces to achieve key properties like invertibility [Lipman and Funkhouser 2009; Schmidt et al. 2019].

In contrast, here we consider the problem of mapping *volumes* to *volumes* rather than surfaces to surfaces. Volumetric correspondence is beneficial for several tasks. In graphics and CAD, boundary representations of shapes are used to represent objects, so even

Authors’ addresses: S. Mazdak Abulnaga, abulnaga@mit.edu, Massachusetts Institute of Technology, 77 Massachusetts Ave, Cambridge, Massachusetts, USA, 02139; Oded Stein, ostein@mit.edu, Massachusetts Institute of Technology, 77 Massachusetts Ave, Cambridge, Massachusetts, USA, 02139; Polina Golland, polina@csail.mit.edu, Massachusetts Institute of Technology, 77 Massachusetts Ave, Cambridge, Massachusetts, USA, 02139; Justin Solomon, jsolomon@mit.edu, Massachusetts Institute of Technology, 77 Massachusetts Ave, Cambridge, Massachusetts, USA, 02139.



Mapping Between Two Volumes With Our Method
(Visualized at Different Depths)

Fig. 1. Our method produces low-distortion correspondences between volumes, visualized as checkerboard textures through the sliced volumes.

the input geometry used to evaluate surface-to-surface mapping techniques typically expresses a volumetric domain. Hence, finding volumetric correspondences may improve correspondences of these boundary representations, since volumetric reasoning is needed to preserve thin features with small area-to-volume ratios. In other applications like medical imaging, the acquired data is inherently volumetric, and surface correspondences are simply insufficient.

Volumes do not share many of the geometric properties that have enabled mapping techniques for surfaces, so new approaches are needed. The closest existing methods to volumetric mapping tackle volumetric deformation and parameterization. In these applications, one starts with a volume in its rest pose and deforms the volume to a target domain or to conform to a set of target handle positions in a fashion that minimizes distortion.

These approaches differ from volumetric mapping in several ways. First, volumetric deformation and parameterization methods typically assume a reasonable initial guess (e.g., the source shape) and flexibility in the target domain (e.g., unconstrained geometry away from the handles) or specialize to a single target (e.g., a ball). In contrast, mapping problems often involve geometrically distinct shapes with no reasonable way to initialize a map beyond a sparse set of landmarks.

Furthermore, mapping problems are typically symmetric, in the sense that the computed map should be invariant to the ordering of the source and target domains; there is no notion of a “rest pose” typical in deformation. Consequently, we seek a distortion energy that is symmetric with respect to the source and target.

We propose an algorithm for mapping between volumes represented as tetrahedral meshes. Our method draws insight from 2D

surface mapping and 3D deformation. It builds on the discretization of maps used in a state-of-the-art surface mapping algorithm [Ezuz et al. 2019] but requires new objective functions and optimization methods to be effective. In particular, we propose a set of *symmetrized* distortion energies that are invariant to the domain over which the map is applied and aim to produce inversion-free, low-distortion matchings that conform closely to the boundary (Fig. 1).

Contributions. This paper contributes the following:

- We present a method for computing volumetric correspondences between far-from-isometric shapes by minimizing a symmetric distortion energy.
- We analyze the concept of a *symmetric* distortion energy, which is agnostic to the ordering of source and target domains, and provide a recipe for *symmetrizing* a distortion energy. We propose a set of desirable properties for a symmetric distortion energy and analyze well-known measures of distortion within our framework.
- We demonstrate our method on a diverse dataset of examples, showing that our method reliably extracts correspondences with low distortion.

2 RELATED WORK

Volumetric correspondence poses a new set of challenges that has not been addressed in works that propose surface-based methods. Although relatively few works consider precisely the problem tackled in this paper, we draw insights from surface mapping, volumetric parameterization, and volumetric deformation and focus our review on relevant work on these topics.

Volumetric parameterization and deformation. Parameterization and deformation algorithms provide means of deforming tetrahedral meshes into prescribed poses or domains with minimal distortion.

A *parameterization* is a deformation of a volume to a simpler domain, such as a topological ball [Abulnaga et al. 2021; Garanzha et al. 2021; Paillé and Poulin 2012; Wang et al. 2003; Yueh et al. 2019] or a polycube [Aigerman and Lipman 2013; Fu and Liu 2016; Li et al. 2021; Paillé and Poulin 2012; Wang et al. 2008b; Xia et al. 2010]. The better-studied instance of parameterization in graphics maps two-dimensional surfaces (rather than volumes) into the plane; see [Floater and Hormann 2005; Fu et al. 2021; Sheffer et al. 2007] for discussion of this broad area of research.

In *deformation*, the task is to deform a volume by moving a set of handles to a set of target positions. These methods are often based on physical models of strain [Irving et al. 2004] and aim to produce elastic deformations minimizing a prescribed energy choice [Chao et al. 2010; Fu et al. 2015; Irving et al. 2004; Kovalsky et al. 2014; Müller et al. 2002; Smith et al. 2018, 2019]. See [Gain and Bechmann 2008; Selim and Koomullil 2016; Sieger et al. 2015] for general discussion.

In both problems above, one computes a deformation from the rest pose to the target. Optimization methods are used to match the target while minimizing distortion, where the distortion is measured using an energy that quantifies the deformation of the Jacobian matrix of each tetrahedron. Since these models start with a good initialization, namely the rest pose, one can optimize using a combination of energies with flip-free barriers and a constrained line

search, arriving at solutions that are both flip-free and have low distortion; see e.g. [Smith and Schaefer 2015] for a representative example. In contrast to these past works, we produce maps between far-from-isometric domains without an obvious effective initialization. Consequently, our choice of energies is designed to be resilient to poor initial maps that are not foldover-free.

Volumetric mappings. Some methods consider the task of computing correspondences between volumetric shapes. To our knowledge, all past methods can be understood as special cases of the deformation methods where the task is to extend a fixed boundary map to the interior of a volume.

Kovalsky et al. [2015] present a local-global alternating algorithm targeting maps with bounded distortion. They demonstrate their algorithm on two volumetric correspondence examples and show one example (their Figure 11) where relaxing boundary constraints at the end of the optimization procedure can help recover from minor artifacts. Su et al. [2019] also target computation of foldover-free volumetric maps with prescribed boundary; they optimize for a foldover-free interior with bounded conformal distortion. Their method has impressive levels of efficiency but targets a specific notion of conformal distortion. Stein et al. [2021] propose an operator splitting technique to optimize nonconvex distortion energies to yield a flip-free parameterization; they demonstrate a few examples of volumetric correspondence.

The approaches above require a prescribed boundary map and minimize distortion of the interior. In contrast, our method freely deforms the boundary to minimize distortion and does not need a bijective, orientation-preserving boundary map as an initializer. Indeed, it is not always obvious how to design a boundary map so that the induced volumetric correspondence has low isometric distortion. We also optimize an alternative objective function that targets symmetry and isometry rather than bounded distortion or conformal structure preservation.

A few mapping methods reduce a mapping problem between volumetric domains to a sequence of surface-mapping problems between leaves of foliations of the two domains. Campen et al. [2016] propose a volumetric parametrization approach relying on a foliation. Their algorithm requires the domain to be a topological ball whose tetrahedral mesh is *bishellable*. Cohen and Ben-Chen [2019] describe an alternative method to compute foliations of more-general volumetric domains using a Hele-Shaw flow along a potential function from a Möbius inversion of the domain boundary to a sphere. Unlike these methods that decompose the domain into surfaces, our method does end-to-end optimization of a mapping over an entire volume at once.

Symmetric maps. *Symmetric* mapping methods are invariant to the ordering of the source and target shapes. Several works in 2D surface mapping do so by optimizing for the average of the forward and reverse map distortion [Ezuz et al. 2019; Schmidt et al. 2019; Schreiner et al. 2004].

We use a similar formulation to achieve symmetry. We analyze several common distortion energies symmetrized in this way and show that—surprisingly—the choice of energy can have counterintuitive consequences. In particular, distortion energies that favor

isometry in one direction may not do so when optimizing their symmetrized counterparts.

We develop the concept of a *symmetric* energy that is invariant to the choice of optimization domain over which it is taken, in the sense that the energy of the inverse map matches that of the forward map. Although it is a sensible choice in our setting, we note the term “symmetric” is somewhat overloaded in the parameterization and mapping literature. Several distortion measures have been deemed symmetric because they equally penalize scaling and shrinking, such as the symmetric Dirichlet energy [Schreiner et al. 2004; Smith and Schaefer 2015] and the symmetric ARAP energy [Shtengel et al. 2017]. Our analysis shows that in fact these energies do not necessarily satisfy our notion of symmetry.

Surface maps. Two-dimensional surface mapping can generally be divided into (at least) three sets of approaches: methods that use an intermediate domain, methods that rely on descriptors, and methods that directly extract a map from one mesh into another. We refer the reader to one of several surveys for a broad overview [Li and Iyengar 2014; Sahillioglu 2020; Van Kaick et al. 2011].

The first two groups of approaches cannot be directly extended to the volumetric case. In particular, while Tutte’s parameterization provides a natural means of mapping surfaces bijectively to an intermediate domain and thus provides a natural means of initializing maps in the first category, no such canonical parameterization exists for volumes. Moreover, volumetric geometry descriptors do not appear to be sufficiently reliable for correspondence tasks.

Methods that find correspondences through an intermediate domain employ a bijective parameterization of each input to a simple domain such as the plane [Kraevoy and Sheffer 2004], the sphere [Gotsman et al. 2003; Haker et al. 2000; Lee and Kazhdan 2019], or a quotient manifold [Aigerman and Lipman 2015, 2016; Aigerman et al. 2014, 2015; Bright et al. 2017; Schmidt et al. 2019]. We also note methods like [Kim et al. 2011; Lipman and Funkhouser 2009], which average multiple maps computed in a similar fashion. These approaches admit no obvious extension to volumes. First, the existence of a bijection to a simpler intermediate domain does not always exist. Second, many of these methods require introducing cutting seams [Aigerman et al. 2015], which becomes substantially more difficult in three dimensions. Furthermore, these may not result in low-distortion maps, as minimizing the composition of the maps in the intermediate domain may result in high distortion in the final surface-to-surface map.

The second set of methods computes maps that match descriptors, possibly with added regularization. Descriptors are often distance-based [Bronstein et al. 2008b; Huang et al. 2008], spectral [Jain et al. 2007; Mateus et al. 2008; Ovsjanikov et al. 2010; Vestner et al. 2017], extrinsic [Ankerst et al. 1999; Salti et al. 2014], or a combination [Dubrovina and Kimmel 2011; Kim et al. 2011; Litman and Bronstein 2013]. Many correspondence methods in this category are built on the functional maps framework [Ovsjanikov et al. 2012, 2016], which finds correspondences by matching functions defined on the shapes. Relatively few descriptors are available for volumetric geometry, whose structure is still inherited from the boundary surface.

The third class of approaches directly optimize for inter-surface maps. These methods compute a map between surfaces by matching features or landmarks while minimizing distortion [Ezuz et al. 2019; Mandad et al. 2017; Schreiner et al. 2004; Solomon et al. 2012, 2016].

Ezuz et al. [2019] produce a map between surfaces by minimizing the geodesic Dirichlet energy of the forward and reverse map and encouraging bijectivity through a reversibility energy. Our algorithm extends many of their ideas to the volumetric case. In our case, however, a new algorithm is required; we also show that mapping with volumetric information can improve their surface map (e.g., by correcting orientation).

Medical image registration. Medical image registration is a form of volumetric shape correspondence in Euclidean space. Here, the task is usually to find correspondences between two volumes that are defined on a voxel grid. The correspondence is driven by matching image intensities, for example using mutual information [Klein et al. 2007] or cross-correlation [Avants et al. 2008]. Similar to our formulation, the transformation is governed by any of several regularization terms, for example to compute a diffeomorphic transformation [Beg et al. 2005]. We refer the reader to surveys [Oliveira and Tavares 2014; Sotiras et al. 2013; Viergever et al. 2016]. While both our approach and registration methods aim to find volumetric correspondences, the techniques used in medical image registration are not applicable, as they operate on a voxel grid and are driven by intensity rather than geometry.

3 MAPPING PROBLEM

We develop a volumetric mapping method that is symmetric, in that the resulting maps are invariant to the ordering of the source and target shapes. We compute the map by minimizing an objective function that measures distortion while satisfying a set of constraints. In this section, we investigate the consequences of the symmetry assumption on our algorithmic design.

3.1 Preliminaries

Given two bounded volumes $M_1, M_2 \subset \mathbb{R}^3$ with smooth boundaries $\partial M_1, \partial M_2$, we seek a map $\phi : M_1 \rightarrow M_2$. Several considerations inform our choice of ϕ , detailed below. Note that this problem is not the same as *deformation* (sometimes referred to as “mapping” in past literature), which aims to find a low-distortion deformation of $M_1 \subset \mathbb{R}^3$ given prescribed target positions for a few handles rather than the geometry of M_2 .

Many algorithms for mapping and deformation can be viewed as optimizing a deformation energy of the form

$$E_f[\phi] := \int_{M_1} f(J_\phi(\mathbf{x})) dV(\mathbf{x}), \quad (1)$$

where $J_\phi \in \mathbb{R}^{3 \times 3}$ is the map Jacobian and $dV(\mathbf{x})$ is the volume form on M_1 .

The distortion function $f : \mathbb{R}^{3 \times 3} \rightarrow \mathbb{R}_{\geq 0}$ usually measures local deviation of the map from isometry. Typical choices of deformation energies favor rigidity [Rabinovich et al. 2017]. For example, the as-rigid-as-possible energy functional (ARAP) [Liu et al. 2008] measures the deviation of the Jacobian from the set of rotation matrices

$\text{SO}(3)$:

$$f_{\text{ARAP}}(J) = \min_{R \in \text{SO}(3)} \|J - R\|_F^2.$$

In contrast, the Dirichlet energy functional

$$f_D(J) = \|J\|_F^2$$

favors the as-constant-as-possible map [Schreiner et al. 2004]. Selection of the distortion function is application-dependent. For example, one might choose f that models a physical strain energy for a deformation task. Alternatively, one might select f to encourage injectivity.

In almost all applications, f is chosen to be *rotation invariant*, reflecting the fact that rigid motions of M_1 and M_2 should not affect the computed map. In this case, $f(J)$ is a function of the singular values $\sigma(J)$, the elements of the diagonal matrix Σ in the singular value decomposition (SVD) $J = U\Sigma V^\top$. In a slight abuse of notation, in our subsequent discussion we will use f to denote both a function on matrices in $\mathbb{R}^{3 \times 3}$ and vectors of singular values in \mathbb{R}^3 , with $f(J) := f(\sigma(J))$.

In addition to finding a map with low distortion, we are concerned with finding one that satisfies a desired set of constraints. For example, we can constrain the boundary of the source volume to be mapped to the boundary of the target, i.e. $\phi(\partial M_1) \subset \partial M_2$. We use \mathcal{P} to denote the constrained *feasible set*. One might imagine other constraints, for example ensuring a set of landmark points are mapped to the pre-specified locations, further restricting \mathcal{P} . Moreover, regularizing objective terms, $\text{Reg}[\phi]$ could be added. So, our optimization problem becomes

$$\begin{aligned} \arg \min_{\phi} \quad & \int_{M_1} f(J_\phi(\mathbf{x})) dV(\mathbf{x}) + \text{Reg}[\phi] \\ \text{subject to} \quad & \phi \in \mathcal{P}. \end{aligned} \quad (2)$$

3.2 Symmetrized Energy Functions

For correspondence problems where there is no clear distinction between the rest pose and the target pose, it is desirable for a volumetric correspondence method to be *symmetric*, meaning that it is invariant to the ordering of the “source” domain M_1 and “target” domain M_2 . For example, in medical imaging, this assumption is natural for computing correspondences between the brain shapes of two subjects extracted from magnetic resonance images (MRI). Similar symmetry arises when seeking a correspondence between two humans standing in the same pose.

Following [Ezuz et al. 2019; Schmidt et al. 2019; Schreiner et al. 2004], one simple way to achieve symmetry is to optimize the average of the distortion energy of a map with the distortion energy of its inverse. Ezuz et al. [2019] and Schreiner et al. [2004] use the simplest choice of energies to symmetrize—the Dirichlet energy—while Schmidt et al. [2019] use the symmetric Dirichlet energy to prevent foldovers. Below, we analyze the consequences of using these energies and other possible choices of f not considered in prior work. Surprisingly, our analysis will show that the Dirichlet energy and several other seemingly reasonable choices do *not* yield an effective notion of distortion after symmetrization, leading us to employ an alternative in our technique.

We start by deriving conditions on f that ensure the distortion energy E_f is invariant to the ordering of the source and target. Let M_1 and M_2 be open subsets of \mathbb{R}^n and $\phi : M_1 \rightarrow M_2$ a diffeomorphism between them. We can compute the distortion of the map ϕ by applying Eq. (1) in both directions:

$$E_f[\phi] = \int_{M_1} f(J_\phi(\mathbf{x})) dV_1(\mathbf{x}) \quad (3)$$

$$E_f[\phi^{-1}] = \int_{M_2} f(J_{\phi^{-1}}(\mathbf{y})) dV_2(\mathbf{y}). \quad (4)$$

Pulling back the integral in Eq. (4) to M_1 , we use a change of variables to $\mathbf{y} = \phi(\mathbf{u})$ to show

$$E_f[\phi^{-1}] = \int_{M_1} f(J_{\phi^{-1}}(\phi(\mathbf{u}))) |\det J_\phi(\mathbf{u})| dV_1(\mathbf{u}). \quad (5)$$

By the inverse function theorem,

$$E_f[\phi^{-1}] = \int_{M_1} f\left(\left(J_\phi(\mathbf{u})\right)^{-1}\right) |\det J_\phi(\mathbf{u})| dV_1(\mathbf{u}). \quad (6)$$

For invariance with respect to the integration domain, Eq. (3) must agree with Eq. (6). Matching the integrands,

$$f(J) = |\det J| f(J^{-1}), \quad (7)$$

is sufficient for this equivalence. In terms of the singular values, we obtain

$$f(\sigma) = \left| \prod_{i=1}^n \sigma_i \right| f\left(\frac{1}{\sigma_1}, \dots, \frac{1}{\sigma_n}\right). \quad (8)$$

Here and in our subsequent discussion, we will use n to refer to the dimensionality of the domains M_1, M_2 when the result under discussion applies to maps in any dimension; $n = 3$ in our application. This motivates the following definition:

Definition 3.1 (Symmetric energy). A distortion energy E_f whose distortion function f satisfies Eq. (7)—or Eq. (8) in terms of singular values—is a *symmetric energy*.

Our symmetric energy condition is both necessary and sufficient for symmetric distortion measures, in the following sense:

PROPOSITION 3.2. $E_f[\phi] = E_f[\phi^{-1}]$ for all M_1, M_2 , and ϕ as defined above if and only if f is a symmetric energy.

PROOF. Substituting (7) into (6) shows that any f satisfying (7) automatically satisfies $E_f[\phi] = E_f[\phi^{-1}]$. We now show the converse. Since $E[\phi] = E[\phi^{-1}] \forall M_1, M_2, \phi$ as defined above, we can choose $M_1 = B_1(\mathbf{0}) \subset \mathbb{R}^n$, the open ball of radius 1. Consider any invertible $J \in \mathbb{R}^{n \times n}$, and define a map $\phi(\mathbf{x}) := J\mathbf{x}$, whose Jacobian is given by $J_\phi(\mathbf{x}) = J$. Take $M_2 := \phi(M_1)$. Applying (3),

$$E_f[\phi] = f(J) \cdot \text{vol}(B_1(\mathbf{0})). \quad (9)$$

Similarly, applying (6) yields

$$E_f[\phi^{-1}] = f(J^{-1}) |\det J| \cdot \text{vol}(B_1(\mathbf{0})). \quad (10)$$

Equating Eq. (9) and Eq. (10) and dividing by $\text{vol}(B_1(\mathbf{0}))$ completes the proof. \square

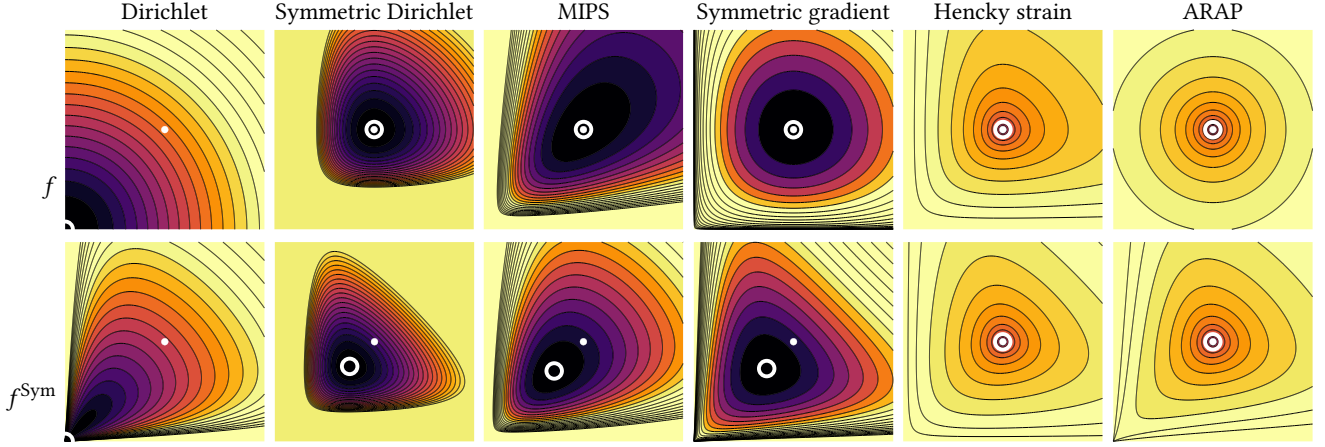


Fig. 2. Level sets of distortion functions f (top) and their symmetrized counterparts f^{Sym} (bottom) evaluated at $(\sigma_1, \sigma_2, 1)$ for $(\sigma_1, \sigma_2) \in [0, 2]^2$. We mark $(1, 1)$ as a white dot and the location of the minimum as a circle. In the parlance of §3.3, all energies except the Dirichlet energy preserve structure (f minimized at $(1, 1, 1)$), while only the Hencky strain and ARAP energies favor isometry (f^{Sym} minimized at $(1, 1, 1)$). Only Dirichlet and ARAP are nonsingular, since the level sets do not diverge as singular values approach 0.

Not all distortion energies are symmetric, but there is a simple procedure to construct a symmetric distortion function f^{Sym} from any distortion function f . For any distortion function f , we can obtain a corresponding f^{Sym} fulfilling Eq. (7) by—in effect—computing $\frac{1}{2}E_f[\phi] + \frac{1}{2}E_f[\phi^{-1}]$ via our symmetrization procedure:

$$f^{\text{Sym}}(J) = \frac{1}{2}f(J) + \frac{1}{2}|\det J|f(J^{-1}), \quad (11)$$

or in terms of singular values,

$$f^{\text{Sym}}(\sigma) = \frac{1}{2}f(\sigma) + \frac{1}{2} \left| \prod_{i=1}^n \sigma_i \right| f\left(\frac{1}{\sigma_1}, \dots, \frac{1}{\sigma_n}\right). \quad (12)$$

For example, suppose $f_D(J) = \|J\|_F^2$ is the distortion function of the Dirichlet energy. Then, the average of the Dirichlet energy of the forward map and of the inverse map yields the distortion function:

$$f_D^{\text{Sym}}(J) = \frac{1}{2}\|J\|_F^2 + \frac{1}{2}|\det J|\|J^{-1}\|_F^2, \quad (13)$$

or for $n = 3$,

$$f_D^{\text{Sym}}(\sigma_1, \sigma_2, \sigma_3) = \frac{1}{2} \sum_{i=1}^3 \sigma_i^2 + \frac{1}{2} (\sigma_1 \sigma_2 \sigma_3) \left(\sum_{j=1}^3 \sigma_j^{-2} \right) \quad (14)$$

Note that this is not the “symmetric” Dirichlet energy from past work on parameterization [Rabinovich et al. 2017; Smith and Schaefer 2015], which has the form $\frac{1}{2}\|J\|_F^2 + \frac{1}{2}\|J^{-1}\|_F^2$. Incidentally, in 2D, the second term in Eq. (13) is the objective function of the inverse harmonic mapping problem used to obtain foldover-free mappings by Garanzha et al. [2021].

Eq. (13) is a model for the objective function for mapping surfaces in [Ezuz et al. 2019; Schreiner et al. 2004], and one could reasonably attempt to reuse the same formulation for volumes. More careful examination of this function, however, indicates some undesirable properties. In particular, as illustrated in Fig. 2, the distortion function $f_D^{\text{Sym}}(\sigma)$ is not minimized at $(1, 1, 1)$, the singular values of

a rigid map. That is, the distortion function of the symmetrized Dirichlet energy f_D^{Sym} favors non-isometric maps, even though it is symmetric.

The counterintuitive behavior of energies like in Eq. (13) suggests that algorithms optimizing the sum of the distortion of a map and the distortion of its inverse can have unpredictable behavior, even for standard choices of distortion functions. We examine this effect empirically in §6.5.

3.3 Designing Symmetric Distortion Energies

In practice, our algorithm maintains separate estimates of the map $\phi : M_1 \rightarrow M_2$ and its inverse $\psi \approx \phi^{-1} : M_2 \rightarrow M_1$, and optimizes an energy of the form $\frac{1}{2}E_f[\phi] + \frac{1}{2}E_f[\psi]$; even if f is not symmetric, the resulting energy is roughly of the form in Eq. (11) and hence our analysis in §3.2 applies.

Several properties are desirable when selecting f :

- Favors isometry: f^{Sym} is minimized at $(1, 1, 1)$.
- Preserves structure: f is minimized at $(1, 1, 1)$.
- Nonsingular: f is defined for all matrices.

Favoring isometry and preserving structure are similar but not identical conditions, and they are desirable for different reasons. Distortion energy functions that favor isometry are the typical choice for geometry processing applications, and this condition simply expresses a preference for maps ϕ that are rigid. On the other hand, structure-preserving choices of f facilitate optimization routines like ours that alternate between estimating ϕ and ψ , ensuring that both alternating steps work toward a common goal. Similarly, nonsingular functions f avoid the need for barrier optimization techniques and feasible initialization.

The following proposition provides a necessary condition that can be used to rule out many standard choices of f when considering the properties above:

PROPOSITION 3.3. Suppose a differentiable function $f : \mathbb{R}_{\geq 0}^3 \rightarrow \mathbb{R}_{\geq 0}$ favors isometry and preserves structure, i.e., $f(\sigma)$ and f^{Sym} are minimized at $(1, 1, 1)$. Then, $f(1, 1, 1) = 0$ and $\nabla f(1, 1, 1) = (0, 0, 0)$.

PROOF. Structure preservation immediately implies $\nabla f(1, 1, 1) = (0, 0, 0)$ since $(1, 1, 1)$ is a local minimum. Similarly, to favor isometry, we must have that $\nabla f^{\text{Sym}}(1, 1, 1) = (0, 0, 0)$. Taking the derivative of (12) in one singular value σ_i , we find

$$\frac{\partial f^{\text{Sym}}}{\partial \sigma_i} = \frac{1}{2} \frac{\partial f}{\partial \sigma_i} + \frac{1}{2} \left| \prod_{j \neq i} \sigma_j \right| \left[f\left(\frac{1}{\sigma_1}, \dots, \frac{1}{\sigma_n}\right) - \frac{1}{|\sigma_i|} \frac{\partial f}{\partial \sigma_i}\left(\frac{1}{\sigma_1}, \dots, \frac{1}{\sigma_n}\right) \right].$$

Substituting $\sigma_1 = \dots = \sigma_n = 1$,

$$0 = \frac{\partial f^{\text{Sym}}}{\partial \sigma_i}(1, \dots, 1) = \frac{1}{2} f(1, \dots, 1).$$

This expression yields our first condition. \square

The result above may feel somewhat counterintuitive, since constant shifts in f affect whether f favors isometry. But, adding a constant to f changes the effect of the volume form on the deformation energy, explaining the result above.

In Table 1, we list several distortion functions $f(J)$, their equivalent forms in terms of the Jacobian J 's singular values $f(\sigma)$, and their symmetrized forms $f^{\text{Sym}}(J)$, $f^{\text{Sym}}(\sigma)$. We check if the symmetrized distortion functions satisfy the isometry favoring property above by examining the behavior of σ_{\min} , the singular values that minimize $f^{\text{Sym}}(\sigma)$. We verify the other properties in a similar way by studying $f(\sigma)$. Table 2 summarizes the result. Figure 2 visualizes these properties by showing level sets of f and f^{Sym} for examples drawn from Table 1.

Tables 1 and 2 reveal several valuable properties that can inform our choice of f . None of the distortion energies in Table 1 is symmetric in its standard form. A surprising result is that, after symmetrization, no distortion energy except for ARAP and Hencky strain favors isometry. Despite the fact that minimizing these energies in the forward or reverse direction independently would lead to an isometry, minimizing for the average of the two does not (see Fig. 2). For example, the symmetric Dirichlet energy and the AMIPS energy after symmetrization prefer maps that tend to shrink ($\sigma_{\min} < 1$). We also observe that the symmetrized Dirichlet and the symmetrized MIPS energies favor maps that collapse, that is, they are minimized close to $\sigma_{\min} \approx (0, 0, 0)$. While the (asymmetric) Dirichlet energy favors maps with $\sigma = 0$, the MIPS energy does not.

From Table 2, only the symmetrized ARAP energy, which we will refer to as *sARAP*, satisfies all the desired properties. To implement the *sARAP* energy, we optimize the average of the ARAP energy of the forward and reverse maps. This objective function has the added benefit of removing the requirement of a flip-free initialization, which is often not available for correspondence tasks.

REMARK (AVOIDING ZERO SINGULAR VALUES). The symmetric Dirichlet energy [Smith and Schaefer 2015], symmetric gradient energy [Stein et al. 2021], and others used for bijective parameterization blow up as singular values approach zero; this property provides a barrier ensuring existence of a locally-optimal parameterization without collapsed or inverted elements. Our nonsingular property actually prefers the opposite of this scenario, allowing inverted Jacobians so that we can

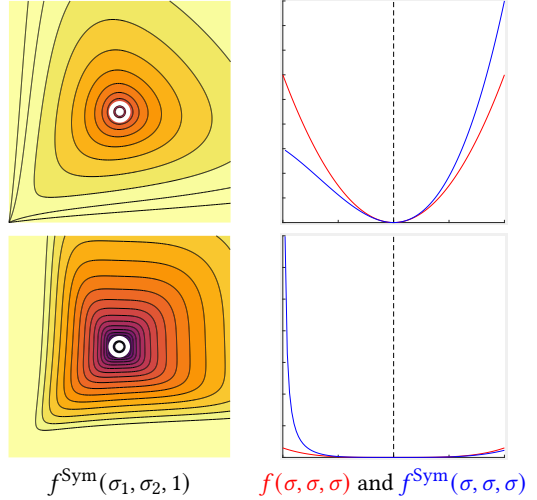


Fig. 3. Mathematical boundary case: Comparison of symmetrized ARAP energy $\sum_i (\sigma_i - 1)^2$ to symmetrized fourth-power ARAP energy $\sum_i (\sigma_i - 1)^4$, using level sets similar to Figure 2 (left) and by plotting the diagonal where $\sigma = \sigma_1 = \sigma_2 = \sigma_3$ (right). As discussed in §3.3 (Remark), the fourth-power alternative blows up when approaching $(0, 0, 0)$ from any direction, while conventional ARAP admits a path to $(0, 0, 0)$ where the energy density remains finite.

recover from poor initialization, but this is a property of f —employed during optimization—rather than f^{Sym} , the actual distortion energy being optimized in the symmetrized formulation.

A nonsingular f can actually admit a function f^{Sym} that blows up as singular values approach 0, as is the case for the ARAP and Dirichlet energies. This property suggests that even a nonsingular choice of f can favor orientation-preserving symmetric maps.

For completeness, we note that $f_{\text{ARAP}}^{\text{Sym}}$ is not a perfect barrier, in the following sense (also illustrated in Figure 3): For $\sigma_1 = 1$ and $\sigma_2, \sigma_3 \rightarrow 0$, we have $f_{\text{ARAP}}^{\text{Sym}}(\sigma) \rightarrow 1$. This technicality can be addressed using an f that grows faster than cubically in the singular values, e.g. $f(\sigma) = \sum_i (\sigma_i - 1)^4$, but in practice such an adjustment did not yield better maps.

REMARK (ROLE OF BOUNDARY CONDITIONS). Several prior works compute maps by optimizing symmetric energies without the desired properties at the beginning of this section [Ezuz et al. 2019; Schmidt et al. 2019; Schreiner et al. 2004]. Although their distortion energies do not promote isometry directly, these methods are still able to find low-distortion and even bijective correspondences. Indeed, the symmetrized energy analysis above does not tell the whole story. In particular, these methods included energy terms, boundary conditions, and other constraints that favor bijectivity and semantic correspondences. We hypothesize that the success of these methods lies in balancing between several competing terms and constraints. We leave detailed theoretical analysis of these intriguing global questions to future work.

3.4 Optimization problem

Following the previous section’s analysis, we revise the the generic formulation of our optimization problem in Eq. (2) to be symmetric, leading to the modified problem:

$$\begin{aligned} \arg \min_{\phi, \psi} \quad & \frac{1}{2} \int_{M_1} f_{\text{ARAP}}(J_\phi(\mathbf{x})) dV(\mathbf{x}) \\ & + \frac{1}{2} \int_{M_2} f_{\text{ARAP}}(J_\psi(\mathbf{y})) dV(\mathbf{y}) + \text{Reg}[\phi, \psi] \end{aligned} \quad (15)$$

subject to $\phi \in \mathcal{P}, \psi \in \mathcal{Q}$,

where \mathcal{Q} denotes the constraint $\psi(\partial M_2) \subset \partial M_1$. In practice, the constraints that define \mathcal{P} and \mathcal{Q} can be made soft and modeled in $\text{Reg}[\phi, \psi]$. The estimate $\psi \approx \phi^{-1}$ can be enforced as a soft or hard constraint. In practice, we use a soft constraint modeled in $\text{Reg}[\phi, \psi]$ as described in §4.3.

4 DISCRETIZATION AND MODEL

We build on our analysis in §3.2 and §3.3 to discretize the optimization problem in Eq. (15) and develop an algorithm to compute a volumetric map that is invariant to the ordering of the source and target shapes. In this section, we define our deformation model, describe our discretized map representation, develop the objective functions used in the optimization, and provide the optimization procedure.

4.1 Notation

We represent volumetric shapes as tetrahedral meshes. We let $\mathcal{V}_i, \mathcal{E}_i, \mathcal{F}_i, \mathcal{T}_i$ denote the sets of vertices, edges, faces, and tetrahedra of mesh M_i , for $i \in \{1, 2\}$. We represent the coordinates of \mathcal{V}_i as a matrix $V_i \in \mathbb{R}^{n_i \times 3}$, where n_i denotes the number of vertices in mesh M_i . We represent tetrahedron k in mesh i as the matrix $V_i^{T_k} \in \mathbb{R}^{4 \times 3}$ whose rows are the coordinates of the vertices of tetrahedron k . We use ∂ to denote the boundary of a mesh, and $\partial\mathcal{V}_i, \partial\mathcal{E}_i, \partial\mathcal{F}_i, \partial\mathcal{T}_i$ denote sets of boundary vertices, edges, faces, and tetrahedra, respectively. Boundary tetrahedra are those that contain one or more boundary faces.

We model the maps ϕ and ψ as piecewise affine, with each tetrahedron being mapped affinely. The map on each tet is determined by its transformed vertex coordinates. We use matrix $X_i \in \mathbb{R}^{n_i \times 3}$ to denote the coordinates of the transformed vertices of mesh M_i , and $X_i^{T_k} \in \mathbb{R}^{4 \times 3}$ to denote the transformed tetrahedron k of mesh M_i . The Jacobian matrix

$$J(X_i^{T_k}) = \left(BX_i^{T_k} \right) \left(BV_i^{T_k} \right)^{-1} \quad (16)$$

defines the deformation of tetrahedron k based on the transformed coordinates $X_i^{T_k}$. The constant matrix $B \in \mathbb{R}^{3 \times 4}$ extracts vectors parallel to the edges of the tetrahedron.

4.2 Map Representation

We wish to constrain each map to lie within the target shape, i.e., $\phi(M_1) \subset M_2$ and $\psi(M_2) \subset M_1$. We extend the strategy of Ezuz et al. [2019] to tetrahedral meshes to enforce these constraints.

We represent the map ϕ as a matrix $P_{12} \in [0, 1]^{n_1 \times n_2}$ and the map ψ as $P_{21} \in [0, 1]^{n_2 \times n_1}$. Suppose P_{12} maps vertex i of mesh

M_1 into tetrahedron $T_k = (a, b, c, d) \in \mathcal{T}_2$ in mesh M_2 , where $(a, b, c, d) \in \{1, \dots, n_2\}$ are the indices of the vertices of T_k . Then, row i of P_{12} contains the barycentric coordinates of the image of vertex i in columns a, b, c, d , and zeros elsewhere. Map P_{21} is constructed analogously. We can enforce the constraint that boundary vertices are mapped to boundary faces by constraining the sparsity patterns of P_{12} and P_{21} .

We denote the set of all feasible maps satisfying the boundary constraints as \mathcal{P}_{ij}^\star ; we use \mathcal{P}_{ij} to denote the set of feasible maps that may map the boundary ∂M_i to the interior of M_j .

We use half-quadratic splitting [Geman and Yang 1995] to express our problem in a form that is amenable to efficient optimization [Ezuz et al. 2019; Wang et al. 2008a; Zoran and Weiss 2011]. In particular, we introduce the auxiliary variable X_{ij} to model the image of vertices \mathcal{V}_i under the map to mesh M_j , where $X_{ij} \approx P_{ij}V_j$.

4.3 Objective Terms

We define several objective terms to govern the shape deformation and model the soft constraints on the map.

4.3.1 Auxiliary and reversibility energy functions. Our first two terms are adapted from Ezuz et al. [2019] and extended for volumetric meshes. The first term is the auxiliary energy that encourages $X_{ij} \approx P_{ij}V_j$:

$$E_Q[P_{12}, P_{21}, X_{12}, X_{21}] = \sum_{\substack{i, j \in \{1, 2\} \\ i \neq j}} \frac{1}{c_i c_j} \|X_{ij} - P_{ij}V_j\|_{M_i}^2, \quad (17)$$

where c_i, c_j are the total volumes of meshes M_i and M_j , and $\|\cdot\|_{M_i}^2$ denotes the Frobenius norm with respect to M_i . For a matrix G , $\|G\|_{M_i}^2 = \text{tr}(G^T C_i G)$, where C_i is the lumped diagonal vertex mass matrix of M_i .

The second term is the reversibility energy that encourages bijectivity:

$$E_R[P_{12}, P_{21}, X_{12}, X_{21}] = \sum_{\substack{i, j \in \{1, 2\} \\ i \neq j}} \frac{1}{c_i^2} \|P_{ij}X_{ji} - V_i\|_{M_i}^2. \quad (18)$$

This energy measures the distance between the original vertex positions V_i and the back projection of their image under the map P_{ij} , X_{ij} .

4.3.2 ARAP energy. Central to the computation of a volumetric map is the proper selection of a distortion energy. From our analysis

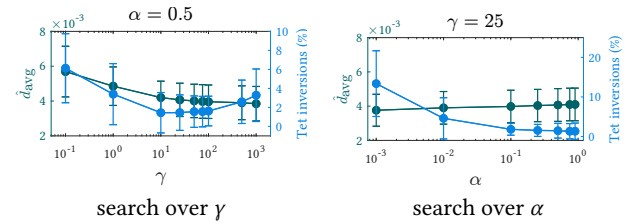


Fig. 4. Parameter sweep over γ and α , comparing the tradeoff between \hat{d}_{avg} and the percentage of tetrahedron inversions. We select $\alpha = 0.5, \gamma = 25$ as they achieve a reasonable tradeoff between conforming to the target boundary while minimizing the number of flipped tetrahedra.

Table 1. Several distortion measures and their symmetrized forms. In this table, we consider orientation-preserving maps, so that $|\det J| = \det J$. We use an interior-point method constrained to search over non-negative σ to compute the set of singular values σ_{\min} that minimize the symmetrized energy $f^{\text{Sym}}(\sigma)$.

Name	$f(J)$	$f(\sigma)$	$f^{\text{Sym}}(J)$	$f^{\text{Sym}}(\sigma)$	σ_{\min}
Dirichlet	$\ J\ _F^2$	$\sum_{i=1}^n \sigma_i^2$	$\frac{1}{2} \ J\ _F^2 + \frac{1}{2} (\det J) \left(\ J^{-1}\ _F^2 \right)$ $+ \frac{1}{2} \left(\prod_{i=1}^n \sigma_i \right) \left(\sum_{k=1}^n \sigma_k^{-2} \right)$	$\frac{1}{2} \sum_{i=1}^n \sigma_i^2$	$\approx (0, 0, 0)$
Symmetric Dirichlet	$\ J\ _F^2 + \ J^{-1}\ _F^2$	$\sum_{i=1}^n (\sigma_i^2 + \sigma_i^{-2})$	$\frac{1}{2} (\det J + 1) \left(\ J\ _F^2 + \ J^{-1}\ _F^2 \right)$	$\frac{1}{2} \left(\prod_{i=1}^n \sigma_i + 1 \right) \left(\sum_{j=1}^n (\sigma_j^2 + \sigma_j^{-2}) \right)$	$\approx (0.73, 0.73, 0.73)$
MIPS (3D)	$\frac{1}{8} \left(\ J\ _F^2 \cdot \ J^{-1}\ _F^2 - 1 \right)$	$\frac{1}{8} \prod_{i=1}^3 \left(\frac{\sigma_i}{\sigma_{i+1}} + \frac{\sigma_{i+1}}{\sigma_i} \right)$	$\frac{1}{16} (\det J + 1) \left(\ J\ _F^2 \cdot \ J^{-1}\ _F^2 - 1 \right)$	$\frac{1}{16} \left(1 + \prod_{i=1}^3 \sigma_i \right) \left(\prod_{j=1}^3 \left(\frac{\sigma_{j+1}}{\sigma_j} + \frac{\sigma_j}{\sigma_{j+1}} \right) \right)$	$\approx (0, 0, 0)$
AMIPS (3D)	$\frac{1}{16} \left(\ J\ _F^2 \cdot \ J^{-1}\ _F^2 - 1 \right)$ $+ \frac{1}{2} (\det J + (\det J)^{-1})$	$\frac{1}{16} \prod_{i=1}^3 \left(\frac{\sigma_i}{\sigma_{i+1}} + \frac{\sigma_{i+1}}{\sigma_i} \right)$ $+ \frac{1}{2} \left(\prod_{j=1}^3 \sigma_j + \prod_{k=1}^n \sigma_k^{-2} \right)$	$\frac{\det J + 1}{32} \left(\ J\ _F^2 \cdot \ J^{-1}\ _F^2 - 1 \right)$ $+ \frac{1}{4} (\det J + (\det J)^{-1})$ $+ \frac{1}{4} ((\det J)^2 + 1)$	$\frac{1}{32} \left(1 + \prod_{i=1}^3 \sigma_i \right) \left(\prod_{j=1}^3 \left(\frac{\sigma_{j+1}}{\sigma_j} + \frac{\sigma_j}{\sigma_{j+1}} \right) \right)$ $+ \frac{1}{4} \left(\prod_{k=1}^3 \sigma_k + \prod_{l=1}^n \sigma_l^{-2} \right)$ $+ \frac{1}{4} \left(\prod_{m=1}^3 \sigma_m^2 \right)$	$\approx (0.8, 0.8, 0.8)$
Conformal AMIPS	$\frac{\text{tr}(J^T J)}{(\det J)^{\frac{2}{3}}}$	$\left(\prod_{j=1}^3 \sigma_j^{-\frac{2}{3}} \right) \left(\sum_{i=1}^3 \sigma_i^2 \right)$	$\frac{1}{2} (\det J)^{-\frac{2}{3}} \text{tr}(J^T J)$ $+ \frac{1}{2} (\det J)^{\frac{1}{3}} \text{tr}(J^{-T} J^{-1})$	$\frac{1}{2} \left(\prod_{i=1}^3 \sigma_i^{-\frac{2}{3}} \right) \left(\sum_{j=1}^3 \sigma_j^2 \right)$ $+ \frac{1}{2} \left(\prod_{k=1}^3 \sigma_k^{-\frac{1}{2}} \right) \left(\sum_{l=1}^3 \sigma_l^{-2} \right)$	$\approx (0.032, 0.032, 0.032)$
Symmetric gradient	$\frac{1}{2} \ J\ _F^2 - \log(\det J)$	$\frac{1}{2} \sum_{j=1}^n \sigma_j^2 - \log \left(\prod_{i=1}^n \sigma_i \right)$	$\frac{1}{4} \ J\ _F^2 - \frac{1}{2} \log(\det J)$ $+ \frac{1}{4} \det J \cdot \ J^{-1}\ _F^2$ $+ \frac{1}{8} \det J \cdot \log(\det J)$	$\frac{1}{4} \sum_{i=1}^n \sigma_i^2 - \frac{1}{2} \log \left(\prod_{j=1}^n \sigma_j \right)$ $+ \frac{1}{4} \left(\prod_{k=1}^n \sigma_k \right) \left[\sum_{l=1}^n \sigma_l^{-2} \right]$ $+ \frac{1}{2} \log \left(\prod_{m=1}^n \sigma_m \right)$	$\approx (0.61, 0.61, 0.61)$
Hencky strain	$\ \log J^T J\ _F^2$	$\sum_{i=1}^n \log^2(\sigma_i)$	$\frac{1}{2} \ \log J^T J\ _F^2$ $+ \frac{1}{2} \det J \cdot \ \log J^{-1}\ _F^2$	$\frac{1}{2} \sum_{i=1}^n \log^2(\sigma_i)$ $+ \frac{1}{2} \left(\prod_{j=1}^n \sigma_j \right) \left(\sum_{k=1}^n \log^2(\sigma_k) \right)$	(1,1,1)
ARAP	$\ J - R\ _F^2$	$\sum_{i=1}^n (\sigma_i - 1)^2$	$\frac{1}{2} \ J - R\ _F^2$ $+ \frac{1}{2} \det J \cdot \ J^{-1} - R\ _F^2$	$\frac{1}{2} \sum_{i=1}^n (\sigma_i - 1)^2$ $+ \frac{1}{2} \left(\prod_{j=1}^n \sigma_j \right) \left(\sum_{k=1}^n (\sigma_k^{-1} - 1)^2 \right)$	(1, 1, 1)

Table 2. Summary of distortion energy function properties

Name	Favors isometry	Preserves structure	Nonsingular
Dirichlet	✗	✗	✓
Symm. Dirichlet	✗	✓	✗
MIPS (3D)	✗	✓	✗
AMIPS (3D)	✗	✓	✗
Conformal AMIPS	✗	✓	✗
Symm. Gradient	✗	✓	✗
Hencky strain	✓	✓	✗
ARAP	✓	✓	✓

in §3.3, we select the sARAP energy as it is both symmetric and promotes rigidity.

We use $\frac{1}{2}E_{\text{ARAP}}[\phi] + \frac{1}{2}E_{\text{ARAP}}[\psi]$ to approximate $E_{\text{sARAP}}[\phi]$. We approximate the integral over the volumetric domain by measuring the distortion energy per tetrahedron. For tetrahedron k of mesh i , the ARAP distortion function is given by

$$f_{\text{ARAP}} \left(J \left(X_{ij}^{T_k} \right) \right) = \sum_{j=1}^3 (\sigma_{k,j} - 1)^2, \quad (19)$$

where $\sigma_{k,j}$ is the j^{th} signed singular value of $J(X_{ij}^{T_k})$. We use the convention laid out by Irving et al. [2004] to define the signed singular value decomposition unambiguously. For $J = U\Sigma V^T$, this convention allows the sign of the smallest singular value σ_{\min} to be negative, $\text{sign}(\sigma_{\min}) = \text{sign}(\det J)$, and $U, V \in \text{SO}(3)$.

The total ARAP energy is then

$$E_{\text{ARAP}}[X_{12}, X_{21}] = \sum_{\substack{i,j \in \{1,2\} \\ i \neq j}} \frac{1}{2c_i} \sum_{T_k \in \mathcal{T}_i} v(T_k) f_{\text{ARAP}} \left(J \left(X_{ij}^{T_k} \right) \right), \quad (20)$$

where $v(T_k)$ denotes the volume of tetrahedron k .

4.3.3 Projection Energy. We encourage preserving the boundary of the source and target meshes by using forward and backward projection energies. We compute the forward projection energy $E_{P,f}$ as

$$E_{P,f}[X_{12}, X_{21}] = \sum_{\substack{i,j \in \{1,2\} \\ i \neq j}} \frac{1}{s_i} \left\| (X_{ij})_{\partial M_i} - \text{proj} \left((X_{ij})_{\partial M_i}, \partial M_j \right) \right\|_{\partial M_i}^2, \quad (21)$$

where $\text{proj} \left((X_{ij})_{\partial M_i}, \partial M_j \right)$ denotes the Euclidean projection of the boundary vertices of ∂M_i with coordinates X_{ij} onto the boundary mesh ∂M_j , s_i denotes the total surface area of ∂M_1 and $\|\cdot\|_{\partial M_i}^2$ denotes the Frobenius norm with respect to boundary triangle mesh ∂M_i .

The backward projection energy $E_{P,b}$ is given by

$$E_{P,b}[X_{12}, X_{21}] = \sum_{\substack{i,j \in \{1,2\} \\ i \neq j}} \frac{1}{s_i} \left\| V_i - \text{proj} \left(V_i, \partial F_j(X_{ji}) \right) \right\|_{\partial M_i}^2, \quad (22)$$

where $\partial F_j(X_{ji})$ denotes the boundary of mesh M_j with vertices given by X_{ji} .

The full projection energy is then

$$E_P[X_{12}, X_{21}] = E_{P,f}[X_{12}, X_{21}] + E_{P,b}[X_{12}, X_{21}]. \quad (23)$$

4.4 Optimization Problem

Combining the deformation energies and constraints, our optimization problem becomes

$$\begin{aligned} & \arg \min_{P_{12}, P_{21}, X_{12}, X_{21}} E[P_{12}, P_{21}, X_{12}, X_{21}] \\ & \text{subject to } P_{12} \in \mathcal{P}_{12}, P_{21} \in \mathcal{P}_{21}, \end{aligned} \quad (24)$$

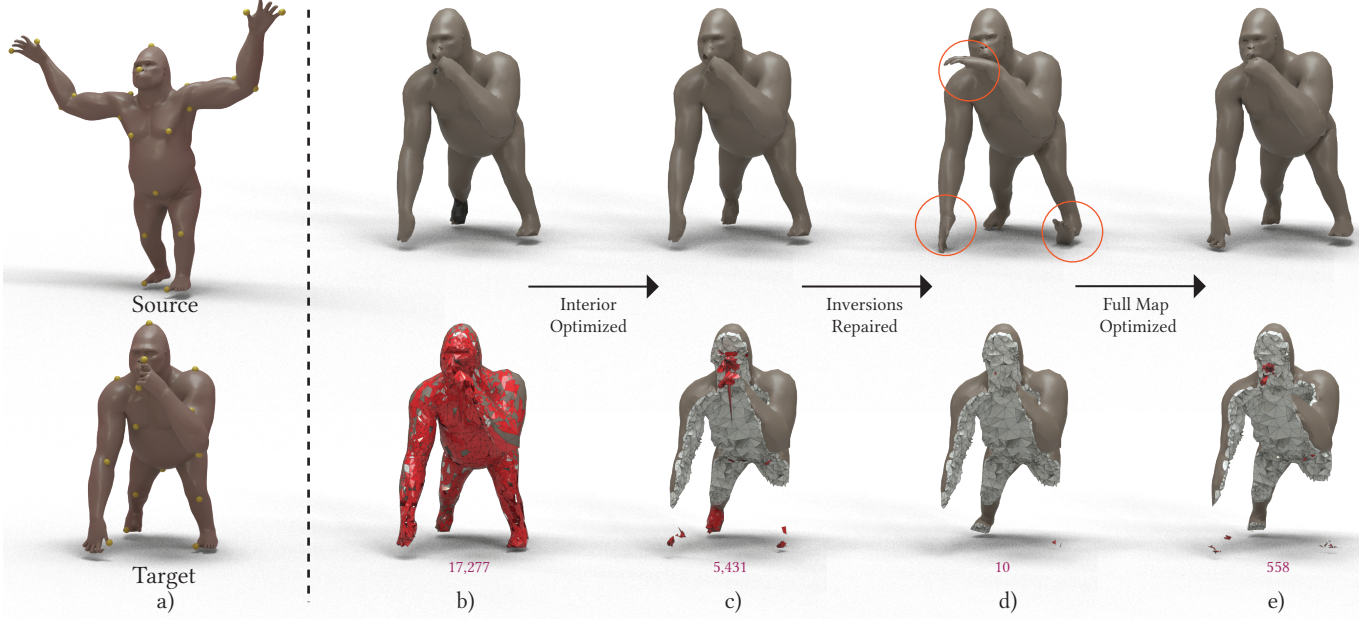


Fig. 5. Flowchart depicting each step of our method: a) initial source and target shapes, with landmarks shown as yellow spheres; mapped shape b) at initialization; c) after optimization converges while keeping the boundary fixed; d) after tetrahedron inversion repair; and e) at convergence. Top row shows the boundary of the mapped shape at every step and the bottom row shows a cut through the interior, revealing interior tetrahedra. Inverted and collapsed tetrahedra are red. The number of inverted tetrahedra is listed under each cut-through mesh. Our initial map b) has all interior tetrahedra collapsed to the boundary, resulting in 17,277 (46%) degenerate or flipped tetrahedra. Steps c) and d) optimize and repair the interior, resulting in 10 flipped tets. The tetrahedron repair step restores elements of the map to match the source, as the hands and feet rotate. The final optimization produces a map that closely matches the boundary with a small number of inversions (558 or 1.5%).

where

$$\begin{aligned}
 E[P_{12}, P_{21}, X_{12}, X_{21}] = & \\
 \sum_{\substack{i,j \in \{1,2\} \\ i \neq j}} \alpha E_{ARAP}[X_{ij}] + (1 - \alpha) E_R[P_{ij}, X_{ji}] & (25) \\
 + \gamma E_P[X_{ij}] + \beta E_Q[X_{ij}, P_{ij}].
 \end{aligned}$$

Several parameters govern the strength of the distortion energies and soft constraints. The parameter $\alpha \in [0, 1]$ models the tradeoff between a reversible map ($\alpha \rightarrow 0$) and one that maintains the rest shape ($\alpha \rightarrow 1$). The parameter $\gamma \in \mathbb{R}_{\geq 0}$ weighs the projection term that models the soft constraint for matching to the target boundary. The parameter β controls the soft constraint on the auxiliary variables. As recommended by [Ezuz et al. 2019; Wang et al. 2008a], β should use an update schedule tailored per application. In our experiments, since we start with a coarse initialization of the interior, we initialize $\beta = 0.25$ and increase β linearly to 5 over 20 iterations. We found our approach to be insensitive to the update schedule.

In this formulation, we use a soft constraint measured by E_P to map to the target boundary. While we could use a hard constraint by setting $\gamma = 0$ and requiring $P_{12} \in \mathcal{P}_{12}^*$, $P_{21} \in \mathcal{P}_{21}^*$, we did not find that this hard constraint had a substantial effect on our final output.

5 OPTIMIZATION

In this section, we outline our optimization procedure. We discuss strategies for initializing the map and propose an approach to uninvert tetrahedra. We conclude by presenting our algorithm for minimizing Eq. (24) using block coordinate descent.

5.1 Initialization

Objective function (24) includes four variables: P_{12} , P_{21} , X_{12} , and X_{21} . In this section, we provide strategies for initializing the variables P_{ij} before running our optimization procedure. We initialize the X_{ij} variables via $X_{ij} \leftarrow P_{ij}V_j$.

Landmark-based initialization. If we are given landmark pairs (p_i, q_i) , where $p_i \in M_1$, $q_i \in M_2$, we can initialize each landmark's target by copying the target of its closest landmark.

2D surface map initialization. A second approach is to initialize the boundaries of M_1 , M_2 using an existing surface-to-surface mapping approach. We initialize the interior vertices identically to landmark-based initialization, where we consider *every* boundary vertex to be a landmark.

5.2 Alternating Minimization

We use coordinate descent, alternating between optimizing over X_{ij} and P_{ij} . Our multi-step optimization procedure ensures strong conformation to the boundary while avoiding inverted tetrahedra.

Optimizing for X_{ij} . Optimizing for X_{ij} while holding the P_{ij} variables fixed is a smooth optimization problem, for which we use the L-BFGS algorithm [Zhu et al. 1997].

We compute the gradient of each energy term in Eq. (25). The gradients for E_P, E_Q are straightforward as they are matrix norms. We compute the gradient of E_{ARAP} using the chain rule. First, we compute the gradient of $f_{ARAP}(J)$ with respect to a Jacobian J ,

$$\nabla J f_{ARAP}[J] = U \text{diag}(\nabla_\sigma f_{ARAP}(\sigma)) V^T.$$

Using the chain rule, we then compute the gradient with respect to the elements of tetrahedron $T_k \in \mathcal{T}_i$, with coordinates $X_{ij}^{T_k}$,

$$\frac{\partial f_{ARAP}(X_{ij}^{T_k})}{\partial (X_{ij}^{T_k})} = \left(\left(BV_i^{T_k} \right)^{-T} B \right) \left(U \text{diag}(\nabla_\sigma f_{ARAP}(\sigma)) V^T \right)^T \quad (26)$$

The gradient with respect to each vertex is found by gathering the gradients of each tetrahedron adjacent to that vertex.

Optimizing for P_{ij} . Fixing X_{12}, X_{21} , the remaining energy terms with respect to P_{ij} are of the form $\|P_{ij}A - B\|_{M_i}^2$, with $A \in \mathbb{R}^{n_j \times 6}, B \in \mathbb{R}^{n_i \times 6}$. Following Ezuz et al. [2019], this minimization can be understood as a *projection* problem solved independently for each row of P_{ij} .

In our case, we need to project the points in A to the 6-dimensional tetrahedral mesh with vertices B , whose connectivity is the same as M_j . The presence of several additional energy terms in our formulation also leads to a unique projection problem. Since the problem can be solved independently, we implement an efficient solution using CUDA programming. To enforce a hard boundary-to-boundary constraint, we map rows of A corresponding to the boundary of M_i to the boundary of the target embedding.

5.3 Inverted Tetrahedron Repair

The initial maps suggested in §5.1 are straightforward to compute, but they are quite distant from our desired output; indeed, the majority of tetrahedra in our initial maps have zero volume. Although alternating between the two steps above is guaranteed to decrease the objective function in each step, empirically we find in the initial stages our algorithm can get stuck in local optima due to inverted elements. Here, we describe a heuristic strategy that empirically can improve the quality of our output.

In this tetrahedron repair step, we find all inverted tetrahedra. We then take the 1-ring neighborhood of the vertices in the inverted tetrahedra and use LBFGS to minimize f_{ARAP} with the remaining vertices fixed.

5.4 Full Algorithm and Stopping Criteria

Overall, our optimization procedure follows four broad steps:

- (1) map initialization (§5.1);
- (2) optimization while keeping the boundary fixed (§5.2);
- (3) inverted tetrahedron repair (§5.3); and
- (4) optimization of all vertices (§5.2).

For stages 2 and 4, we set as our convergence criteria one of (i) the norm of the gradient $< 10^{-6}$, (ii) the objective function decreases by less than 10^{-9} between successive iterations, or (iii) run for

Algorithm 1 Coordinate decent with tetrahedra uninversion

Input: initial maps P_{12}, P_{21}

Output: optimized maps P_{12}, P_{21}

```

1:  $\partial P_{12}^{(0)} \leftarrow P_{12}(\partial V_1, :) // initial boundary map$ 
2:  $\partial P_{21}^{(0)} \leftarrow P_{21}(\partial V_2, :)$ 
3:  $X_{12} \leftarrow P_{12}V_2 // initial vertex map$ 
4:  $X_{21} \leftarrow P_{21}V_1$ 
5:
6: while !converged do // optimize boundary map
7:   for  $(i, j) \in \{(1, 2), (2, 1)\}$  do
8:      $P_{ij} \leftarrow \arg \min_{P \in \mathcal{P}_{ij}} \bar{E}_R[P, X_{ji}] + \bar{E}_Q[P, X_{ij}]$ 
9:      $X_{ij} \leftarrow \arg \min_{X \in \mathbb{R}^{n_i \times 6}} \bar{E}_{ARAP}[X_{ij}]$ 
          $+ \bar{E}_R[X_{ij}, P_{ji}] + \bar{E}_P[X_{ij}] + \bar{E}_Q[X_{ij}, P_{ij}]$ 
10:     $\partial P_{ij} \leftarrow \partial P_{ij}^{(0)} // restore boundary$ 
11:
12:   // inverted tetrahedron repair
13:    $\text{idx} \leftarrow \det J(X_i^{T_k}) \leq 0, \forall T_k \in \mathcal{T}_i // find inverted tetrahedra$ 
14:    $X_{ij}(\text{idx}) \leftarrow \arg \min_{X \in \mathbb{R}^{n_i \times 6}} \bar{E}_{ARAP}[X_{ij}(\text{idx})] // 1\text{-ring nbhd.}$ 
15:
16:   while !converged do // optimize full map
17:     for  $(i, j) \in \{(1, 2), (2, 1)\}$  do
18:        $P_{ij} \leftarrow \arg \min_{P \in \mathcal{P}_{ij}} \bar{E}_R[P, X_{ji}] + \bar{E}_Q[P, X_{ij}]$ 
19:        $X_{ij} \leftarrow \arg \min_{X \in \mathbb{R}^{n_i \times 6}} \bar{E}_{ARAP}[X_{ij}]$ 
          $+ \bar{E}_R[X_{ij}, P_{ji}] + \bar{E}_P[X_{ij}] + \bar{E}_Q[X_{ij}, P_{ij}]$ 

```

50 iterations; the third criterion is a fallback that rarely occurs in practice.

Algorithm 1 summarizes our full procedure.

5.5 Implementation Details

Unless otherwise noted, all figures are generated using identical parameters. We use grid search to identify reasonable parameters; the results of our analysis are provided in Fig. 4. We set the rigidity parameter $\alpha = 0.5$ and the boundary conformation parameter $\gamma = 25$, achieving a reasonable trade off between average distance to the target and percentage of tetrahedron inversions. To find these values, we initialize $\beta = 0.25$ and increase linearly to $\beta = 5$ over 20 iterations. In practice, we found our method was insensitive to the choice of β .

We generate tetrahedral meshes using fTetWild [Hu et al. 2020]. Prior to mapping, we normalize each mesh to have volume 1. We perform one tetrahedron repair step as we found negligible improvement after performing more.

We implement our method in MATLAB, using CUDA to optimize the projection step by extending the projection code in [Li et al. 2021] to \mathbb{R}^6 .

6 EXPERIMENTS

We measure map quality by assessing distortion and closeness to matching the target shapes (§6.1). We validate our method by mapping pairs of shapes from four datasets (§6.2) and report visualizations and numerical scores evaluating the result (§6.3). We also compare possible strategies for initialization (§6.4), highlighting

Table 3. Quantitative results on all mesh pairs in our dataset. Our maps closely match the target boundaries while producing low distortion and few tetrahedron inversions. Here, ℓ denotes the number of landmarks. Time is measured in minutes.

Names	ℓ	$ \mathcal{T}_i $		Time	% inversions		% bdry. inversions		\hat{d}_{\max}		\hat{d}_{avg}		$ \det \hat{J} $		
scan_011	scan_019	23	36420	43527	50.3	1.79	1.65	1.72	1.57	0.0644	0.0666	0.00436	0.00491	0.958±0.108	0.95±0.118
scan_011	scan_030	19	36420	37588	23.2	1.06	0.564	1.04	0.564	0.0554	0.0705	0.00433	0.00493	0.964±0.0828	0.968±0.0683
scan_019	scan_039	16	43527	50713	35.5	1.08	1.39	1.05	1.29	0.0518	0.0622	0.00429	0.00459	0.955±0.107	0.952±0.116
B313 placenta_1	B313 placenta_2	7	151522	158977	105	0.066	0.703	0.0601	0.626	0.108	0.112	0.00887	0.00963	0.98±0.032	0.974±0.0732
C307 placenta (p.1)	C307 placenta (p.2)	5	64837	105693	187	0.273	1.29	0.23	1.06	0.0782	0.0844	0.00782	0.00751	0.964±0.0507	0.951±0.094
G308 placenta_100	G308 placenta_1	12	162762	177523	187	1.63	5.08	1.53	4.35	0.0719	0.0717	0.00549	0.00557	0.96±0.109	0.962±0.076
airplane1	airplane2	7	24894	30700	40.6	0.245	1.92	0.233	1.83	0.0375	0.0522	0.00262	0.0031	0.958±0.0891	0.909±0.186
armadillo	def. armadillo	21	81114	113794	69.2	0.0616	0.611	0.0616	0.606	0.0968	0.0969	0.00351	0.00345	0.98±0.0365	0.975±0.0476
bird_1	bird_2	12	30361	90810	27.2	0.0527	0.268	0.0527	0.255	0.0464	0.0402	0.00405	0.00408	0.982±0.0344	0.964±0.0649
cat0	cat1	17	17867	22988	18.7	0.509	0.761	0.504	0.713	0.0734	0.0665	0.00485	0.00435	0.976±0.0613	0.971±0.066
cat4	cat5	18	25985	22710	28.5	1.37	0.387	1.24	0.374	0.0719	0.0747	0.00526	0.00544	0.966±0.0826	0.971±0.0619
centaur0	centaur1	37	30357	26954	22.7	0.135	1.14	0.135	1.05	0.0679	0.0731	0.00417	0.00456	0.983±0.0353	0.978±0.0551
dancer	dancer2	13	58535	36902	86.9	2.56	1.52	2.28	1.49	0.0228	0.0244	0.00197	0.00231	0.864±0.236	0.916±0.166
dog4	dog5	27	31469	30160	29.7	1.03	1.1	0.963	1.05	0.0634	0.0647	0.00413	0.00425	0.962±0.0975	0.967±0.0844
dog6	dog7	24	26739	43771	60.3	1.75	3.18	1.7	3	0.0856	0.0652	0.00509	0.00418	0.945±0.111	0.923±0.161
dog7	dog8	25	81145	85128	92.8	0.535	1.17	0.531	1.11	0.0865	0.0893	0.00405	0.00427	0.985±0.0371	0.982±0.0573
dolphin_t	shark_t	9	129443	55440	59.6	5.77	10.1	3.63	7.86	0.0481	0.0785	0.00798	0.0149	0.732±0.363	0.718±0.413
dragon_stand	dragonstand2	28	109823	194651	30.8	0.00728	0.878	0.00455	0.87	0.0809	0.0824	0.00359	0.00364	0.993±0.0145	0.987±0.0317
fish1	fish2	8	64410	58215	167	4.33	1.5	4.06	1.41	0.0844	0.0728	0.00431	0.00394	0.916±0.211	0.95±0.124
glass1	glass2	13	30921	13439	25.9	3.95	2.21	3.84	2.21	0.02	0.0203	0.00273	0.00185	0.813±0.269	0.843±0.169
gorilla1	gorilla5	26	37417	59375	66.5	1.49	1.03	1.43	0.979	0.0812	0.0607	0.00579	0.00435	0.978±0.0535	0.963±0.0781
horse0	horse5	16	31507	34978	38.1	0.181	0.469	0.181	0.386	0.0863	0.0895	0.00439	0.00485	0.981±0.0603	0.979±0.0455
cow_t	horse_t	21	31694	32515	35.9	1.26	3.42	1.09	2.61	0.0869	0.114	0.00568	0.00614	0.954±0.111	0.951±0.107
human1	human2	21	56550	82581	81.8	0.401	2.09	0.394	2.04	0.0499	0.0628	0.00294	0.00352	0.973±0.0599	0.971±0.0709
michael0	michael7	20	19445	30014	30.7	0.453	1.65	0.453	1.6	0.0499	0.0399	0.00365	0.00289	0.985±0.0399	0.98±0.0526
seahorse2	seahorse4	22	13720	15667	13.9	0.19	0.702	0.19	0.702	0.0699	0.06	0.00365	0.0031	0.986±0.0419	0.984±0.0359
toy1	toy2	12	75236	62880	49.1	0.106	0.398	0.102	0.347	0.127	0.131	0.00554	0.00553	0.975±0.0524	0.966±0.0788

that our method is robust to poor initial estimates, and we compare the difference in performance by choosing the sARAP energy over the symmetrized Dirichlet energy (§6.5).

6.1 Quality Metrics

We validate our method using the metrics outlined below.

Boundary matching. We measure fit to the target boundary using the Hausdorff distance d_{\max} and the chamfer distance d_{avg} defined as follows:

$$d_{\max}(M_1, M_2) = \max \left\{ \sup_{x \in M_1} \inf_{y \in M_2} d(x, y), \sup_{y \in M_2} \inf_{x \in M_1} d(x, y) \right\} \quad (27)$$

$$d_{\text{avg}}(M_1, M_2) = \frac{1}{|\mathcal{V}_1| + |\mathcal{V}_2|} \left[\sum_{v_i \in \mathcal{V}_1} d(v_i, M_2) + \sum_{v_j \in \mathcal{V}_2} d(v_j, M_1) \right]. \quad (28)$$

Here, \mathcal{V}_1 and \mathcal{V}_2 denote the sets of vertices of M_1 and M_2 , respectively. To make the measures above scale-independent, we normalize both quantities by the length of the diagonal of the bounding box enclosing the target mesh. We use hats to denote normalized quantities: \hat{d}_{\max} and \hat{d}_{avg} .

To visualize the distortion in the interiors of tetrahedral meshes, we use a mapped checkerboard pattern. In each map visualization, using Houdini, we slice the source shape with a plane and place an extrinsic checkerboard pattern on the intersection, using rounding and modulo operations on coordinates. We push forward the planar intersection surface through our map and render the result using a custom shader that looks back to the corresponding coordinate in the source and evaluates the checkerboard function. Interpolation happens by finding the closest element (xyzdist) and then transferring coordinates (primuv).

Distortion and inversion. We measure the quality of the transformation by computing the percent of inverted tetrahedra as well as the mean normalized Jacobian determinant $\det \hat{J}$ (weighted by tetrahedron volume), where the columns of J are normalized as in [Li et al. 2021]. Figures containing qualitative results depict distortion per tetrahedron using the ARAP energy $\sum_{i=1}^3 (|\sigma_i| - 1)^2$.

6.2 Datasets

We evaluate our method on 24 mesh pairs from four datasets. For datasets where only triangle meshes are available, we tessellate the interiors. We randomly select pairs of shapes distorted non-isometrically from the SHREC19 dataset [Dyke et al. 2019]. We also randomly select matching and non-matching pairs of humans and animals for nonrigid correspondence from the TOSCA dataset [Bronstein et al. 2008a]. Finally, we obtain tetrahedral meshes of models of natural objects and CAD models from [Fu et al. 2016; Li et al. 2021], from Thingi10k [Zhou and Jacobson 2016], and from Thingiverse [Japan 2022]. We manually choose landmarks on the boundary surfaces for every mapping example (marked on most figures); Table 3 provides the number of landmarks for each pair.

6.3 Validation

In this section, we demonstrate our maps on several pairs.

Algorithm flowchart. We demonstrate each step of our algorithm in Fig. 5. First, we compute an initial boundary map using the method of Ezuz et al. [2019]. This initial map is interpolated from the boundary to the interior by mapping each interior vertex to the target of its closest boundary vertex, as described in §5.1. This procedure results in a significant number of inverted or collapsed tetrahedra (Fig. 5b). The interior is then improved by minimizing the map energy over the interior vertices (Fig. 5c). Then, we repair inverted tetrahedra, dramatically reducing the number of flipped tetrahedra, as described

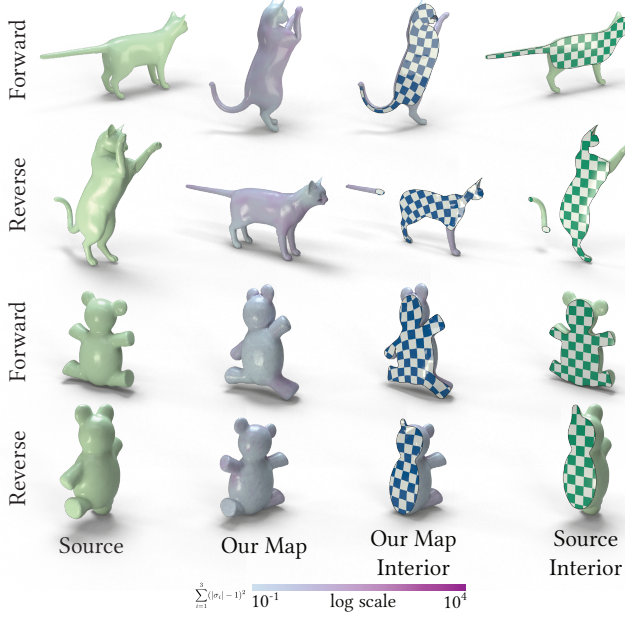


Fig. 6. Forward and reverse maps on related pairs of shapes. We observe smooth patterns of distortion on the boundary while capturing distinguishing geometric features, such as the deformation of the tail of the cat and movement of the bear’s ears. Distortion is uniform throughout the interior.

in §5.3. We see the mapped mesh start to restore its source pose; the hands and feet rotate (Fig. 5c). We compute the final map by optimizing over all vertices. We arrive at a solution that closely conforms to the target boundary while minimizing distortion (Fig. 5e).

Map results. We demonstrate our method on several pairs of domains. Fig. 6 shows the forward and reverse maps between pairs of deformations from the same domain. In both examples, distortion is smooth throughout the boundary, and our map successfully matches geometric features, for example the curved tail and the ears in the cat pairs. The checkerboard patterns demonstrate that our maps are smooth in the interior.

Fig. 7 shows results for the more challenging problem of mapping between pairs of shapes from different domains. Distortions are mainly smooth on the boundary but are expectantly high in regions of large deformation, e.g., in the nose and rudder of the airplane in the forward direction. Here, the volume of the nose has to shrink substantially while the rudder has to expand in height. Similarly, we see large distortion in the cow-horse pair, particularly in the ears in the reverse map and in the knees and feet in the forward map. Our boundary term yields maps that closely conform to the target at the cost of greater tetrahedral distortion and some inverted elements.

Table 3 presents quantitative results for mappings on all pairs of data. Our maps consistently perform well across all pairs in our dataset. They closely match the boundary, with $\hat{d}_{\text{avg}} < 6 \cdot 10^{-3}$ and $\hat{d}_{\text{max}} < 0.15$ for all pairs. Our maps effectively preserve tetrahedron quality, with mean $\det \hat{J} > 0.9$ for all but one pair, and the majority of pairs having fewer than 2% flipped tetrahedra. The majority (95%)

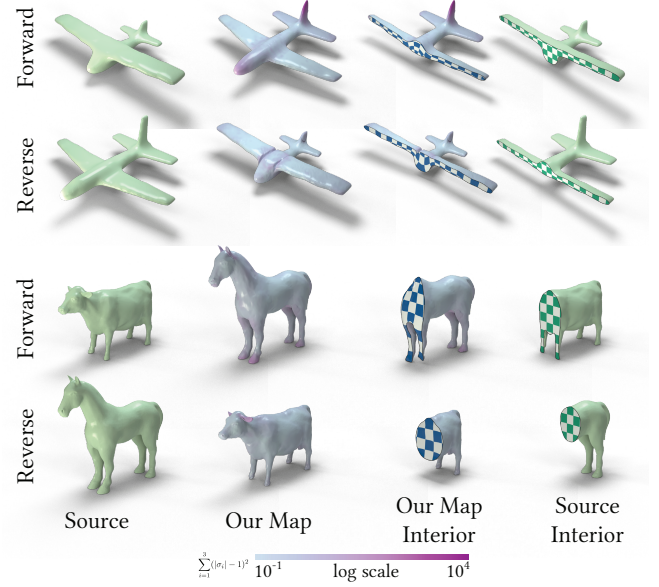


Fig. 7. Forward and reverse maps on far-from-isometric shapes. Our maps capture the extreme deformations, for example by growing and collapsing the airplane rudder and deforming the ears of the horse and cow pair. Matching boundary features expectantly leads to large deformation, as a large volume change is required to model these transformations. The checkerboard pattern reveals that interior deformation is affected by large boundary distortions (see airplane) but is uniform and smooth elsewhere.

of flipped tetrahedra lie on the boundary, indicating that inversions occur when trying to conform to sharp boundary features.

6.4 Initialization

Here, we study the effect of and alternatives for the initialization procedure (§5.1) as well as our algorithm’s resilience to poor initialization.

Fig. 8 shows how our algorithm recovers artifacts in the 2D surface map initialization procedure (§5.1). Starting from our landmarks, [Ezuz et al. 2019] results in parts of the surface that are folded inside out (the backs of triangles are shown in black), as seen on the arms and legs of the human and the paws of the dog; the initial maps also have collapsed boundary features (hand of the human, tail of the dog). Since our method targets orientation-preserving maps, we correct these inverted areas. Furthermore, since our method is volumetric, we fill the tail of the dog as well as the hands and feet of the human.

Fig. 9 demonstrates our resultant map when initialized using a sparse set of landmark points (§5.1, landmark-based initialization). While the initial map is unintelligible, our output matches the target shape closely. The final map has low distortion throughout the boundary and captures the narrow features of the target, including the fingers and bends in the legs. Furthermore, the checkerboard pattern reveals uniform distortion in the interior.



Fig. 8. Refinement of the initial boundary map using [Ezuz et al. 2019]. The backs of triangles on the boundary are shown in black. The initial map produces areas of the surface turned inside out and collapses regions like the hands of the human and tail of the dog. Since our method targets orientation-preserving correspondences and is volumetric, we restore collapsed regions and produce a consistent orientation of the boundary. Further, this experiment reveals that our method can recover from poor initialization.

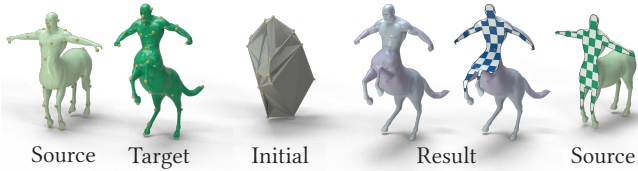


Fig. 9. Resulting map when initialized using only a sparse set of landmark points. Despite an initialization that collapses the mesh to a set of landmarks, we produce a map that captures sharp geometric features of the target including the hands and bends of the legs. We see the distortion is smooth and uniform throughout the boundary and interior.

These experiments demonstrate that our method is resilient to the choice of initialization. We do not depend strongly on an initial bijective boundary map and can use a landmark-only based approach.

6.5 Symmetrized Energy Choice

We experiment with the choice of symmetrized energy and its effect on producing a map. As described in §3.3, several symmetrized energies do not favor isometry while our choice, the sARAP energy, does. Fig. 10 compares the output when optimizing using the sARAP and symmetrized Dirichlet (sDir) energies. In these experiments, we remove the tetrahedron repair step, which made the artifacts we uncover even worse. We compare two choices of γ and visualize the resultant maps.

The sDir energy completely collapses the map for $\gamma = 0.1$, since the projection term has little effect at keeping the map intact. Similarly, parts of the mapped mesh degenerate with $\gamma = 25$. In contrast,

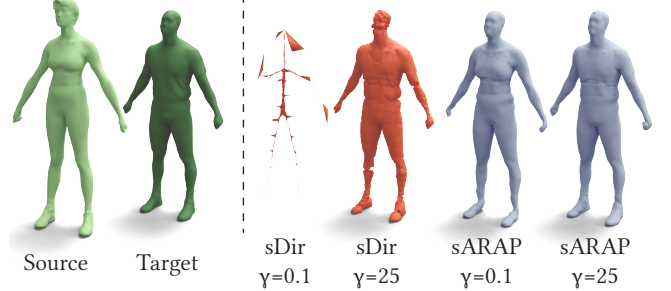


Fig. 10. Comparison of maps when optimizing with the symmetrized Dirichlet (sDir) and sARAP energies. sDir produces collapsed maps for both values of γ , although $\gamma = 25$ keeps parts of the map intact as it pushes vertices to the boundary. The sARAP energy does not lead to a collapse, but starts to show the source shape for $\gamma = 0.1$, as expected.

the sARAP energy does not produce a collapsed map, although it starts to restore the source when $\gamma = 0.1$.

This experiment verifies our analysis in §3.2 and additionally shows that methods using energies that do not favor isometry can be sensitive to parameter choice.

7 EXAMPLES

Volumetric maps are useful for transporting data between domains. Below, we depict some use cases that would benefit from our low-distortion, near-diffeomorphic maps.

7.1 Internal geometry transfer

In contrast to pulling back functions on M_2 to M_1 , we can also push forward maps into M_1 to M_2 . This category of data includes point clouds, collections of curves $[0, 1] \rightarrow M_1$, and arbitrary subdomains $U \subset M_1$.

As an example of how data can be easily transported using our maps, in Fig. 11 we push forward integral curves of a frame field on domain M_1 through $\phi : M_1 \rightarrow M_2$. The frame fields and their integral curves were generated using ARFF [Palmer et al. 2020]. Integral curves were pushed forward by mapping the curve vertices individually using piecewise linearity. The integral curves remain nearly orthogonal under the map, showing that it is close to isometric. The pushed-forward integral curves closely match the integral curves computed directly on M_2 , also reflecting the map’s degree of metric preservation.

In a second example, we simulate an internal geometry transfer task. As shown in Fig. 12, we place several objects representing anatomy inside of our source mesh and push these forward to our target. We see that despite rotation of the head and movement of the arm, structure is largely maintained. For the meshes used in this example we credit [Averin 2017; Leemhuis 2018; Medical 2013; Reininger 2015; YEG 3D Printing 2015].

7.2 Hex mesh transfer

Our maps can transport other volumetric structures. Hexahedral meshing remains difficult and often requires extensive human intervention; our maps can transport expensive-to-compute hex meshes

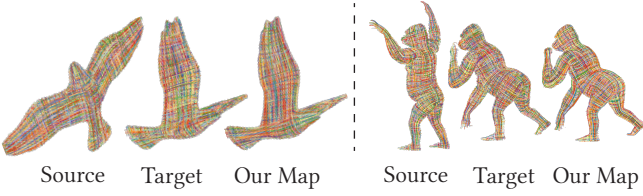


Fig. 11. When the integral curves of an octahedral frame field are pushed forward from a source domain (left) to a target domain (right), the result looks similar to the integral curves of a field computed directly on the target (center). The mapped curves remain nearly orthogonal, illustrating the low metric distortion of our map.

between domains. Fig. 13 transports a hexahedral mesh designed using the method of Li et al. [2021] on one domain to a deformed domain. Similar to how we push forward integral curves, we transport a hex mesh by mapping its vertices individually, maintaining the combinatorial structure of the mesh. Due to the low metric distortion of the map, the distortion of most of the hexahedra remains low, as measured by the scaled Jacobian. However, the right foot of the mapped hex mesh has two toes joined together. This artifact is caused by projection to the wrong boundary target, an artifact also encountered by Li et al. [2021]; as their approach has user interaction, they suggest adding landmarks during the optimization to clarify difficult targets.

7.3 Volumetric data transfer

We demonstrate one example of volumetric data transfer using a dataset of placentas extracted from fetal MRI [Abulnaga et al. 2021]. The mapping is done on data from two patients. The first mapped pair contains two scans acquired where the mother is lying in two positions: supine and left lateral. The second contains two scans acquired ~ 10 minutes apart. Fig. 14 presents the results. The figure marks one important anatomical landmark, a cotyledon, which is responsible for the exchange of blood from the maternal side to the fetal side [Benirschke and Driscoll 1967]. Cotyledons appear as hyperintense circular regions in MRI. We observe close correspondence in the placental geometry. We see similar patterns in the mapped texture and the target. We leave to future work a detailed study of our method’s relevance to MRI data.

8 DISCUSSION

We successfully map a collection of shapes of diverse geometry and demonstrate that our maps closely match the target boundary with low distortion throughout the volume. Our method is robust to the choice of initialization (Figs. 8 and 9) and can produce a dense correspondence even when starting with a low-quality, many-to-one map (Fig. 9). Our examples illustrate scenarios that require a volumetric correspondence, namely internal geometry transfer, hex mesh transfer, and volumetric data transfer.

Key to the development of our algorithm was the analysis of symmetric distortion energies in §3.2-3.3. We symmetrized several common distortion energies and found that only the sARAP energy had the desirable properties of favoring isometry, preserving structure, and being nonsingular. We provide a simple way to symmetrize



Fig. 12. Internal geometry transfer. We place several objects representing human anatomy in the interior of our source mesh and push these forward to the target using our volumetric map.

a distortion energy and check if it satisfies these properties. Fig. 10 also shows that some choices of energy can lead to degenerate maps that are sensitive to the parameters used. The nonsingularity of the sARAP energy is favorable for computing a map given a degenerate initializer. Since volumetric correspondence has no obvious initializer, this property is key in our target applications, as we can recover from poor initialization. Additional work remains in designing symmetric distortion energies that satisfy even more desirable properties.

8.1 Limitations

We observed a few failure cases as can be seen in Fig. 15. First, we encountered shapes where finding a volumetric map was simply infeasible. In the screw threads example, the required map would have to add or remove a large amount of volume, which would lead to substantial distortion. Furthermore, the threads on the boundary differ in number, making it impossible to match sharp features. In the second case, we were unable to map a shark with a cavity in its interior to a dolphin with a solid interior. The cavity is a large hollow area to which a volumetric approach is highly sensitive. Furthermore, our method is unable to map between domains of different genus; our examples focus only on genus-0 topology. Last, as demonstrated in Fig. 13, our method can join together small features in the boundary (e.g., armadillo toes). This artifact is caused by an incorrect boundary projection. A potential fix would be to have soft landmark constraints in the optimization.

Our solutions also had a small number of flipped tetrahedra. While our tetrahedron repair step was able to fix almost all inversions, some remained in our final map. The significant majority of these lie on the boundary, indicating that we may need a more dense tesselation to match target geometry, especially in challenging cases.

Finally, our method takes between minutes and hours to compute the correspondences. The computational bottleneck is computing the SVD for each tetrahedron many times on the CPU to approximate the gradient of the objective function. A future direction is to improve the convergence time by using a second-order method and to use the GPU for parallelization.

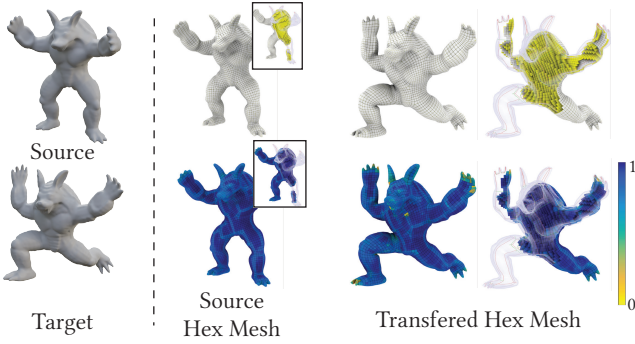


Fig. 13. Hex mesh pushed forward from one volume to another using our map. We observe low distortion, as measured by the scaled Jacobian overall, but there is some distortion in the mapped right foot. Hex meshes are visualized with HexaLab [Bracci et al. 2019], which clamps negative scaled Jacobian values to 0.

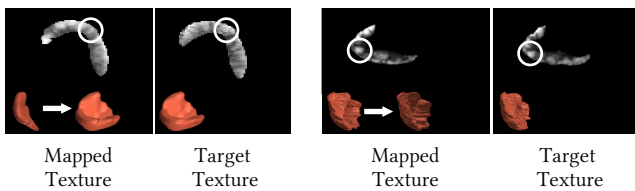


Fig. 14. Volumetric data transfer of two fetal MRI volumes visualized as cross-sections of 3D MRI. The figure shows texture transfer between two volumes in a scenario where the mother is lying in the supine and left lateral position (left), and in a scenario where the two volumes are 10 minutes apart (right). The circle marks the location of a cotyledon in the target texture.

8.2 Future Work

A desirable extension of this work is to correct the inverted tetrahedra in our final map. Inversions are due to two effects: poor tesselation at the boundary resulting in inversions to match narrow features, and differences between the X_{ij} and P_{ij} optimization variables. A new optimization formulation may be required to accomplish the second goal, for example using ADMM.

An exciting future direction is to develop application-specific volumetric correspondences. We provided a few examples of tasks where volumetric correspondence is useful. Our example of mapping MRI signals demonstrated that while matching geometries can improve correspondence, a method that incorporates both the geometry and signal intensities is needed. One framework could be to combine our deformation-based approach with functional maps.

We envision this work to be a starting point for dense volumetric correspondence applicable to a broad set of shapes. The nascent area of volumetric correspondence is largely unexplored, and our theoretical discussion suggests many intriguing mathematical questions and algorithmic design challenges.

ACKNOWLEDGMENTS

This work is funded in part by NIH NIBIB NAC P41EB015902, NIH NICHD R01HD100009, Wistron Corporation, Army Research Office

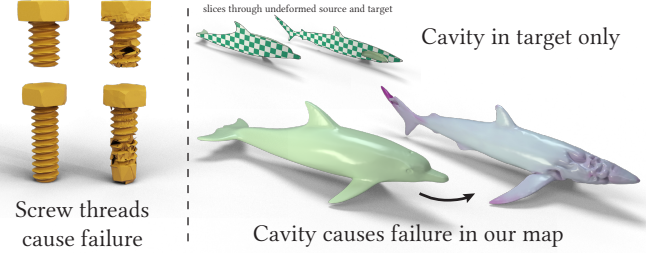


Fig. 15. Limitations. We were unable to map between the screw threads, as the map required removing or adding a large amount of material, leading to significant distortion. In our second example, the target shape, a shark, had a large cavity in its interior, while the source, a dolphin, did not.

grants W911NF2010168 and W911NF2110293, of Air Force Office of Scientific Research award FA9550-19-1-031, of National Science Foundation grants IIS-1838071 and CHS-1955697, from the CSAIL Systems that Learn program, from the MIT-IBM Watson AI Laboratory, from the Toyota-CSAIL Joint Research Center, from a gift from Adobe Systems, and from the Skoltech-MIT Next Generation Program, the Swiss National Science Foundation’s Early Post-doc.Mobility fellowship, the NSF Graduate Research Fellowship, the NSERC Postgraduate Scholarship – Doctoral, and the MathWorks Fellowship.

The authors would also like to thank David Palmer for insightful discussions and help with the frame field and hex mesh transfer experiments. The authors would also like to thank Lingxiao Li for his help in extending the CUDA code for tetrahedron projection in \mathbb{R}^6 . We would also like to thank Yu Wang, Zoë Marschner, Artem Lukoianov, and Ishita Goluguri for their help in proof reading.

REFERENCES

S Mazdak Abulnaga, Esra Abaci Turk, Mikhail Bessmeltsev, P Ellen Grant, Justin Solomon, and Polina Golland. 2021. Volumetric Parameterization of the Placenta to a Flattened Template. *IEEE Transactions on Medical Imaging* (2021).

Noam Aigerman and Yaron Lipman. 2013. Injective and bounded distortion mappings in 3D. *ACM Trans. Graph.* 32, 4 (2013), 106.

Noam Aigerman and Yaron Lipman. 2015. Orbifold Tutte embeddings. *ACM Trans. Graph.* 34, 6 (2015), 1–12.

Noam Aigerman and Yaron Lipman. 2016. Hyperbolic orbifold tutte embeddings. *ACM Trans. Graph.* 35, 6 (2016), 217–1.

Noam Aigerman, Roi Poranne, and Yaron Lipman. 2014. Lifted bijections for low distortion surface mappings. *ACM Trans. Graph.* 33, 4 (2014), 1–12.

Noam Aigerman, Roi Poranne, and Yaron Lipman. 2015. Seamless surface mappings. *ACM Trans. Graph.* 34, 4 (2015), 1–13.

Mihai Ankerst, Gabi Kastenmüller, Hans-Peter Kriegel, and Thomas Seidl. 1999. 3D shape histograms for similarity search and classification in spatial databases. In *International Symposium on Spatial Databases*. Springer, 207–226.

Brian B Avants, Charles L Epstein, Murray Grossman, and James C Gee. 2008. Symmetric diffeomorphic image registration with cross-correlation: evaluating automated labeling of elderly and neurodegenerative brain. *Medical Image Analysis* 12, 1 (2008), 26–41.

Eugeny Averin. 2017. Dog bone. <https://www.thingiverse.com/thing:2090975>

M Faisal Beg, Michael I Miller, Alain Trouvé, and Laurent Younes. 2005. Computing large deformation metric mappings via geodesic flows of diffeomorphisms. *International Journal of Computer Vision* 61, 2 (2005), 139–157.

Kurt Benirschke and Shirley G. Driscoll. 1967. The Pathology of the Human Placenta. In *Placenta*. Springer Berlin Heidelberg, 97–571.

Matteo Bracci, Marco Tarini, Nico Pietroni, Marco Livesu, and Paolo Cignoni. 2019. HexaLab.net: An online viewer for hexahedral meshes. *Computer-Aided Design* 110 (2019), 24–36.

Alon Bright, Edward Chien, and Ofir Weber. 2017. Harmonic global parametrization with rational holonomy. *ACM Trans. Graph.* 36, 4 (2017), 1–15.

Alexander M Bronstein, Michael M Bronstein, Alfred M Bruckstein, and Ron Kimmel. 2008b. Analysis of two-dimensional non-rigid shapes. *International Journal of Computer Vision* 78, 1 (2008), 67–88.

Alexander M Bronstein, Michael M Bronstein, and Ron Kimmel. 2008a. *Numerical geometry of non-rigid shapes*. Springer Science & Business Media.

Marcel Campen, Cláudio T Silva, and Denis Zorin. 2016. Bijective maps from simplicial foliations. *ACM Trans. Graph.* 35, 4 (2016), 1–15.

Isaac Chao, Ulrich Pinkall, Patrick Sanan, and Peter Schröder. 2010. A Simple Geometric Model for Elastic Deformations. *ACM Trans. Graph.* 29, 4 (2010), 38:1–38:6.

David Cohen and Mirela Ben-Chen. 2019. Generalized volumetric foliation from inverted viscous flow. *Computers & Graphics* 82 (2019), 152–162.

Anastasia Dubrovina and Ron Kimmel. 2011. Approximately isometric shape correspondence by matching pointwise spectral features and global geodesic structures. *Advances in Adaptive Data Analysis* 3 (2011), 203–228.

R. M. Dyke, C. Stride, Y.-K. Lai, P. L. Rosin, M. Aubry, A. Boyarski, A. M. Bronstein, M. M. Bronstein, D. Cremers, M. Fisher, T. Groueix, D. Guo, V. G. Kim, R. Kimmel, Z. Lähner, K. Li, O. Litany, T. Remez, E. Rodolà, B. C. Russell, Y. Sahillioglu, R. Slossberg, G. K. L. Tam, M. Vestner, Z. Wu, and J. Yang. 2019. Shape Correspondence with Isometric and Non-Isometric Deformations. In *Eurographics Workshop on 3D Object Retrieval*. The Eurographics Association.

Danielle Ezuz, Justin Solomon, and Mirela Ben-Chen. 2019. Reversible harmonic maps between discrete surfaces. *ACM Trans. Graph.* 38, 2 (2019), 1–12.

Michael S Floater and Kai Hormann. 2005. Surface parameterization: A tutorial and survey. In *Advances in Multiresolution for Geometric Modelling*. Springer Berlin Heidelberg, 157–186.

Xiao-Ming Fu, Chong-Yang Bai, and Yang Liu. 2016. Efficient volumetric polycube-map construction. *Computer Graphics Forum (Pacific Graphics)* 35, 7 (2016).

Xiao-Ming Fu and Yang Liu. 2016. Computing Inversion-Free Mappings by Simplex Assembly. *ACM Trans. Graph.* 35, 6 (2016).

Xiao-Ming Fu, Yang Liu, and Baining Guo. 2015. Computing locally injective mappings by advanced MIPS. *ACM Trans. Graph.* 34, 4 (2015), 71.

Xiao-Ming Fu, Jian-Ping Su, Zheng-Yu Zhao, Qing Fang, Chunyang Ye, and Ligang Liu. 2021. Inversion-free geometric mapping construction: A survey. *Computational Visual Media* 7, 3 (2021), 289–318.

James Gain and Dominique Bechmann. 2008. A survey of spatial deformation from a user-centered perspective. *ACM Trans. Graph.* 27, 4 (2008), 1–21.

Vladimir Garanzha, Igor Kaporin, Liudmila Kudryavtseva, François Protais, Nicolas Ray, and Dmitry Sokolov. 2021. Foldover-free maps in 50 lines of code. *ACM Trans. Graph.* 40, 4 (2021).

D. Geman and Chengda Yang. 1995. Nonlinear image recovery with half-quadratic regularization. *IEEE Transactions on Image Processing* 4, 7 (1995), 932–946.

Craig Gotsman, Xianfeng Gu, and Alla Sheffer. 2003. Fundamentals of spherical parameterization for 3D meshes. *ACM Trans. Graph.* 22, 3 (2003), 358–363.

Steven Haker, Sigurd Angenent, Allen Tannenbaum, Ron Kikinis, Guillermo Sapiro, and Michael Halle. 2000. Conformal surface parameterization for texture mapping. *IEEE Transactions on Visualization and Computer Graphics* 6, 2 (2000), 181–189.

Yixin Hu, Teseo Schneider, Bolun Wang, Denis Zorin, and Daniele Panozzo. 2020. Fast tetrahedral meshing in the wild. *ACM Trans. Graph.* 39, 4 (2020).

Qi-Xing Huang, Bart Adams, Martin Wicke, and Leonidas J Guibas. 2008. Non-rigid registration under isometric deformations. In *Computer Graphics Forum*, Vol. 27. Wiley Online Library, 1449–1457.

Geoffrey Irving, Joseph Teran, and Ronald Fedkiw. 2004. Invertible finite elements for robust simulation of large deformation. In *Proc. 2004 ACM SIGGRAPH/Eurographics Symposium on Computer Animation*, 131–140.

Varun Jain, Hao Zhang, and Oliver Van Kaick. 2007. Non-rigid spectral correspondence of triangle meshes. *International Journal of Shape Modeling* 13, 1 (2007), 101–124.

Yahoo! Japan. 2022. Yahoo! Japan Thingiverse. <https://www.thingiverse.com/yahoojapan/designs>

Vladimir G Kim, Yaron Lipman, and Thomas Funkhouser. 2011. Blended intrinsic maps. *ACM Trans. Graph.* 30, 4 (2011), 1–12.

Stefan Klein, Marius Staring, and Josien PW Pluim. 2007. Evaluation of optimization methods for nonrigid medical image registration using mutual information and B-splines. *IEEE Transactions on Image Processing* 16, 12 (2007), 2879–2890.

Shahar Z Kovalsky, Noam Aigerman, Ronen Basri, and Yaron Lipman. 2014. Controlling singular values with semidefinite programming. *ACM Trans. Graph.* 33, 4 (2014), 68–1.

Shahar Z Kovalsky, Noam Aigerman, Ronen Basri, and Yaron Lipman. 2015. Large-scale bounded distortion mappings. *ACM Trans. Graph.* 34, 6 (2015), 191–1.

Vladislav Kraevoy and Alla Sheffer. 2004. Cross-parameterization and compatible remeshing of 3D models. *ACM Trans. Graph.* 23, 3 (2004), 861–869.

Sing Chun Lee and Misha Kazhdan. 2019. Dense Point-to-Point Correspondences Between Genus-Zero Shapes. In *Computer Graphics Forum*, Vol. 38. Wiley Online Library, 27–37.

Jim Leemhuis. 2018. Programmable animatronic eyeball mechanism demo. <https://www.thingiverse.com/thing:2857377>

Lingxiao Li, Paul Zhang, Dmitry Smirnov, S Mazdak Abulnaga, and Justin Solomon. 2021. Interactive all-hex meshing via cuboid decomposition. *ACM Trans. Graph.* 40, 6 (2021), 1–17.

Xin Li and SS Iyengar. 2014. On computing mapping of 3D objects: A survey. *ACM Computing Surveys (CSUR)* 47, 2 (2014), 1–45.

Yaron Lipman and Thomas Funkhouser. 2009. Möbius voting for surface correspondence. *ACM Trans. Graph.* 28, 3 (2009), 1–12.

Roei Litman and Alexander M Bronstein. 2013. Learning spectral descriptors for deformable shape correspondence. *IEEE Transactions on Pattern Analysis and Machine Intelligence* 36, 1 (2013), 171–180.

Ligang Liu, Lei Zhang, Yin Xu, Craig Gotsman, and Steven J. Gortler. 2008. A local/global approach to mesh parameterization. *Computer Graphics Forum* 27, 5 (2008), 1495–1504.

Manish Mandad, David Cohen-Steiner, Leif Kobbelt, Pierre Alliez, and Mathieu Desbrun. 2017. Variance-minimizing transport plans for inter-surface mapping. *ACM Trans. Graph.* 36, 4 (2017), 1–14.

Diana Mateus, Radu Horaud, David Knossow, Fabio Cuzzolin, and Edmond Boyer. 2008. Articulated shape matching using Laplacian eigenfunctions and unsupervised point registration. In *IEEE Conference on Computer Vision and Pattern Recognition*. IEEE, 1–8.

Prevue Medical. 2013. Lower spine and ribcage from chest CT. <https://www.thingiverse.com/thing:54669>

Matthias Müller, Julie Dorsey, Leonard McMillan, Robert Jagnow, and Barbara Cutler. 2002. Stable real-time deformations. In *Proc. 2002 ACM SIGGRAPH/Eurographics Symposium on Computer Animation*, 49–54.

Francisco PM Oliveira and Joao Manuel RS Tavares. 2014. Medical image registration: A review. *Computer Methods in Biomechanics and Biomedical Engineering* 17, 2 (2014), 73–93.

Maks Ovsjanikov, Mirela Ben-Chen, Justin Solomon, Adrian Butscher, and Leonidas Guibas. 2012. Functional maps: A flexible representation of maps between shapes. *ACM Trans. Graph.* 31, 4 (2012), 1–11.

Maks Ovsjanikov, Etienne Corman, Michael Bronstein, Emanuele Rodolà, Mirela Ben-Chen, Leonidas Guibas, Frederic Chazal, and Alex Bronstein. 2016. Computing and processing correspondences with functional maps. In *SIGGRAPH ASIA 2016 Courses*, 1–60.

Maks Ovsjanikov, Quentin Mérigot, Facundo Mémoli, and Leonidas Guibas. 2010. One point isometric matching with the heat kernel. In *Computer Graphics Forum*, Vol. 29. Wiley Online Library, 1555–1564.

Gilles-Philippe Paillé and Pierre Poulin. 2012. As-conformal-as-possible discrete volumetric mapping. *Computers & Graphics* 36, 5 (2012), 427–433.

David Palmer, David Bommes, and Justin Solomon. 2020. Algebraic representations for volumetric frame fields. *ACM Trans. Graph.* 39, 2, Article 16 (2020).

Michael Rabinovich, Roi Poranne, Daniele Panozzo, and Olga Sorkine-Hornung. 2017. Scalable locally injective mappings. *ACM Trans. Graph.* 36, 4, Article 37a (2017).

Urban Reiningher. 2015. Geared heart. <https://www.thingiverse.com/thing:662447>

Yusuf Sahillioglu. 2020. Recent advances in shape correspondence. *The Visual Computer* 36, 8 (2020), 1705–1721.

Samuele Salti, Federico Tombari, and Luigi Di Stefano. 2014. SHOT: Unique signatures of histograms for surface and texture description. *Computer Vision and Image Understanding* 125 (2014), 251–264.

Patrick Schmidt, Janis Born, Marcel Campen, and Leif Kobbelt. 2019. Distortion-minimizing injective maps between surfaces. *ACM Trans. Graph.* 38, 6 (2019), 1–15.

John Schreiner, Arul Asirvatham, Emil Praun, and Hugues Hoppe. 2004. Inter-surface Mapping. *ACM Trans. Graph.* 23, 3 (2004), 870–877.

MM Selim and RP Koomullil. 2016. Mesh deformation approaches—a survey. *Journal of Physical Mathematics* 7, 2 (2016), 1–9.

Alla Sheffer, Emil Praun, and Kenneth Rose. 2007. Mesh parameterization methods and their applications. *Foundations and Trends in Computer Graphics and Vision* 2, 2 (2007), 105–171.

Anna Shtengel, Roi Poranne, Olga Sorkine-Hornung, Shahar Z Kovalsky, and Yaron Lipman. 2017. Geometric optimization via composite majorization. *ACM Trans. Graph.* 36, 4 (2017), 1–11.

Daniel Sieger, Stefan Menzel, and Mario Botsch. 2015. On shape deformation techniques for simulation-based design optimization. In *New challenges in grid generation and adaptivity for scientific computing*. Springer, 281–303.

Breannan Smith, Fernando De Goes, and Theodore Kim. 2018. Stable neo-hookean flesh simulation. *ACM Trans. Graph.* 37, 2 (2018), 1–15.

Breannan Smith, Fernando De Goes, and Theodore Kim. 2019. Analytic eigensystems for isotropic distortion energies. *ACM Trans. Graph.* 38, 1 (2019), 1–15.

Jason Smith and Scott Schaefer. 2015. Bijective parameterization with free boundaries. *ACM Trans. Graph.* 34, 4, Article 70 (2015), 70:1–70:9 pages.

Justin Solomon, Andy Nguyen, Adrian Butscher, Mirela Ben-Chen, and Leonidas Guibas. 2012. Soft maps between surfaces. In *Computer Graphics Forum*, Vol. 31. Wiley Online Library, 1617–1626.

Justin Solomon, Gabriel Peyré, Vladimir G Kim, and Suvrit Sra. 2016. Entropic metric alignment for correspondence problems. *ACM Trans. Graph.* 35, 4 (2016), 1–13.

Aristeidis Sotiras, Christos Davatzikos, and Nikos Paragios. 2013. Deformable medical image registration: A survey. *IEEE Transactions on Medical Imaging* 32, 7 (2013), 1153–1190.

Oded Stein, Jiajin Li, and Justin Solomon. 2021. A splitting scheme for flip-free distortion energies. arXiv:cs.GR/2107.05200

Jian-Ping Su, Xiao-Ming Fu, and Ligang Liu. 2019. Practical foldover-free volumetric mapping construction. In *Computer Graphics Forum*, Vol. 38. Wiley Online Library, 287–297.

Oliver Van Kaick, Hao Zhang, Ghassan Hamarneh, and Daniel Cohen-Or. 2011. A survey on shape correspondence. In *Computer Graphics Forum*, Vol. 30. Wiley Online Library, 1681–1707.

Matthias Vestner, Zorah Lähner, Amit Boyarski, Or Litany, Ron Slossberg, Tal Remez, Emanuele Rodola, Alex Bronstein, Michael Bronstein, Ron Kimmel, et al. 2017. Efficient deformable shape correspondence via kernel matching. In *International Conference on 3D Vision*. IEEE, 517–526.

Max A. Viergever, J.B. Antoine Maintz, Stefan Klein, Keelin Murphy, Marius Staring, and Josien P.W. Pluim. 2016. A survey of medical image registration—under review, 140–144 pages.

Jiapeng Wang, Shuang Zhao, Xin Tong, Stephen Lin, Zhouchen Lin, Yue Dong, Baining Guo, and Heung-Yeung Shum. 2008b. Modeling and rendering of heterogeneous translucent materials using the diffusion equation. *ACM Trans. Graph.* 27, 1 (2008), 1–18.

Yalin Wang, Xianfeng Gu, Shing-Tung Yau, et al. 2003. Volumetric harmonic map. *Communications in Information & Systems* 3, 3 (2003), 191–202.

Yilun Wang, Junfeng Yang, Wotao Yin, and Yin Zhang. 2008a. A new alternating minimization algorithm for total variation image reconstruction. *SIAM Journal on Imaging Sciences* 1, 3 (2008), 248–272.

Jiazhui Xia, Ying He, Xiaotian Yin, Shuchu Han, and Xianfeng Gu. 2010. Direct-product volumetric parameterization of handlebodies via harmonic fields. In *Shape Modeling International Conference*. IEEE, 3–12.

YEG 3D Printing. 2015. Frankenstein’s monster with removable brain. <https://www.thingiverse.com/thing:1081535>

Mei-Heng Yueh, Tiexiang Li, Wen-Wei Lin, and Shing-Tung Yau. 2019. A novel algorithm for volume-preserving parameterizations of 3-manifolds. *SIAM Journal on Imaging Sciences* 12, 2 (2019), 1071–1098.

Qingnan Zhou and Alec Jacobson. 2016. Thingi10K: A Dataset of 10,000 3D-Printing Models. *arXiv preprint arXiv:1605.04797* (2016).

Ciyou Zhu, Richard H Byrd, Peihuang Lu, and Jorge Nocedal. 1997. Algorithm 778: LBFGS-B: Fortran subroutines for large-scale bound-constrained optimization. *ACM Transactions on mathematical software (TOMS)* 23, 4 (1997), 550–560.

Daniel Zoran and Yair Weiss. 2011. From learning models of natural image patches to whole image restoration. In *2011 International Conference on Computer Vision*. IEEE, 479–486.